Draft version September 23, 2019
Typeset using LaTeX **twocolumn** style in AASTeX62

TOI-503: The first known brown dwarf-Am star binary from the TESS mission*

Ján Šubjak,[1,2] Rishikesh Sharma,[3] Theron W. Carmichael,[4,5,6] Marshall C. Johnson,[7] Henri M. J. Boffin,[8] Rafael Brahm,[9,10,11] Priyanka Chaturvedi,[12] Abhijit Chakraborty,[3] David R. Ciardi,[13] Karen A. Collins,[5] Massimiliano Esposito,[12] Malcolm Fridlund,[14,15] Tianjun Gan,[16] Davide Gandolfi,[17] Rafael A. García,[18,19] Erica J. Gonzales,[20,6] Eike Guenther,[21] Artie Hatzes,[21] Elisabeth Matthews,[22] David W. Latham,[5] Carina M. Persson,[14] Howard M. Relles,[5] Joshua E. Schlieder,[23] Thomas Barclay,[24] Courtney D. Dressing,[25] Ian Crossfield,[22] Andrew W. Howard,[26] Florian Rodler,[27] George Zhou,[5] Samuel N. Quinn,[5] Gilbert A. Esquerdo,[5] Michael L. Calkins,[5] Perry Berlind,[5] Keivan G. Stassun,[28,29] Simon Albrecht,[30] Roi Alonso Sobrino,[31,32] Paul Beck,[31,32,33] Martin Blažek,[1,34] Juan Cabrera,[35] Ilaria Carleo,[36] William D. Cochran,[37] Szilard Csizmadia,[35] Fei Dai,[38,39] Hans J. Deeg,[31,32] Jerome P. de Leon,[40] Philipp Eigmüller,[35] Michael Endl,[37] Anders Erikson,[35] Akai Fukui,[41] Iskra Georgieva,[14] Lucía González-Cuesta,[31,32] Sascha Grziwa,[42] Diego Hidalgo,[31,32] Teruyuki Hirano,[43] Maria Hjorth,[30] Emil Knudstrup,[30] Judith Korth,[42] Kristine W. F. Lam,[44] John H. Livingston,[40] Mikkel N. Lund,[30] Rafael Luque,[31,32] Savita Mathur,[31,32] Pilar Montanes Rodríguez,[31,32] Felipe Murgas,[31,32] Norio Narita,[45,46,41,31] David Nespral,[31,32] Prajwal Niraula,[47] Grzegorz Nowak,[31,32] Enric Pallé,[31,32] Martin Pätzold,[42] Jorge Prieto-Arranz,[31,32] Heike Rauer,[35,48,49] Seth Redfield,[36] Ignasi Ribas,[50,51] Marek Skarka,[1,34] Alexis M. S. Smith,[35] Magdalena Špoková,[1,34] Vincent Van Eylen,[39] and Petr Kabáth[1]

[1]Astronomical Institute, Czech Academy of Sciences, Fričova 298, 251 65, Ondřejov, Czech Republic
[2]Astronomical Institute of Charles University, V Holešovičkách 2, 180 00, Praha, Czech Republic
[3]Astronomy & Astrophysics Division, Physical Research Laboratory, Ahmedabad 380009, India
[4]Harvard University, Cambridge, MA 02138
[5]Center for Astrophysics | Harvard & Smithsonian, 60 Garden Street, Cambridge, MA 02138, USA
[6]National Science Foundation Graduate Research Fellow
[7]Las Cumbres Observatory, 6740 Cortona Drive, Suite 102, Goleta, CA 93117, USA
[8]ESO, Karl-Schwarzschild-Straße 2, 85748 Garching bei München, Germany
[9]Center of Astro-Engineering UC, Pontificia Universidad Católica de Chile, Av. Vicua Mackenna 4860, 7820436 Macul, Santiago, Chile
[10]Instituto de Astrofísica, Pontificia Universidad Católica de Chile, Av. Vicua Mackenna 4860, Macul, Santiago, Chile
[11]Millennium Institute for Astrophysics, Chile
[12]Thüringer Landessternwarte Tautenburg, Sternwarte 5, 07778 Tautenburg, Germany
[13]Caltech/IPAC-NASA Exoplanet Science Institute, M/S 100-22, 770 S. Wilson Ave, Pasadena, CA 91106, USA
[14]Chalmers University of Technology, Department of Space, Earth and Environment, Onsala Space Observatory, SE-439 92 Onsala, Sweden
[15]Leiden Observatory, University of Leiden, PO Box 9513, 2300 RA, Leiden, The Netherlands
[16]Physics Department and Tsinghua Centre for Astrophysics, Tsinghua University, Beijing 100084, China
[17]Dipartimento di Fisica, Università degli Studi di Torino, via Pietro Giuria 1, I-10125, Torino, Italy
[18]IRFU, CEA, Université Paris-Saclay, Gif-sur-Yvette, France
[19]AIM, CEA, CNRS, Université Paris-Saclay, Université Paris Diderot, Sorbonne Paris Cité, F-91191 Gif-sur-Yvette, France
[20]University of California, Santa Cruz, 1156 High Street, Santa Cruz CA 95065, USA
[21]Thüringer Landessternwarte Tautenburg, Sternwarte 5, 07778 Tautenburg, Germany
[22]Department of Physics, and Kavli Institute for Astrophysics and Space Research, Massachusetts Institute of Technology, Cambridge, MA 02139, USA
[23]Exoplanets and Stellar Astrophysics Laboratory, Code 667, NASA Goddard Space Flight Center, Greenbelt, MD 20771, USA
[24]NASA Goddard Space Flight Center, Greenbelt, MD 20771
[25]Astronomy Department, University of California, Berkeley, CA 94720, USA
[26]California Institute of Technology, Pasadena, CA 91125, USA
[27]European Southern Observatory, Alonso de Córdova 3107, Vitacura, Santiago, Chile
[28]*Vanderbilt University, Department of Physics & Astronomy, 6301 Stevenson Center Ln., Nashville, TN 37235, USA*
[29]*Fisk University, Department of Physics, 1000 18th Ave. N., Nashville, TN 37208, USA*
[30]Stellar Astrophysics Centre, Department of Physics and Astronomy, Aarhus University, Ny Munkegade 120, DK-8000 Aarhus C, Denmark
[31]Instituto de Astrofísica de Canarias, C/ Vía Láctea s/n, E-38205 La Laguna, Spain

* This work is done under the framework of the KESPRINT collaboration (`http://kesprint.science`). KESPRINT is an international consortium devoted to the characterisation and research of exoplanets discovered with space-based missions.

[32]Departamento de Astrofísica, Universidad de La Laguna, E-38206 La Laguna, Spain
[33]Institut for Physics, Karl-Franzens University of Graz, Universitätsplatz 5, 8020 Graz, Austria
[34]Department of Theoretical Physics and Astrophysics, Masaryk University, Kotlářská 2, 61137 Brno, Czech Republic
[35]Institute of Planetary Research, German Aerospace Center, Rutherfordstrasse 2, D-12489 Berlin, Germany
[36]Astronomy Department and Van Vleck Observatory, Wesleyan University, Middletown, CT 06459, USA
[37]Department of Astronomy and McDonald Observatory, University of Texas at Austin, 2515 Speedway, Stop C1400, Austin, TX 78712, USA
[38]Department of Physics and Kavli Institute for Astrophysics and Space Research, Massachusetts Institute of Technology, Cambridge, MA 02139, USA
[39]Department of Astrophysical Sciences, Princeton University, 4 Ivy Lane, Princeton, NJ 08544, USA
[40]Department of Astronomy, The University of Tokyo, 7-3-1 Hongo, Bunkyo-ku, Tokyo 113-0033, Japan
[41]National Astronomical Observatory of Japan, 2-21-1 Osawa, Mitaka, Tokyo 181-8588, Japan
[42]Rheinisches Institut für Umweltforschung an der Universität zu Köln, Aachener Strasse 209, D-50931 Köln, Germany
[43]Department of Earth and Planetary Sciences, Tokyo Institute of Technology, 2-12-1 Ookayama, Meguro-ku, Tokio 152-8551, Japan
[44]Zentrum für Astronomie und Astrophysik, Technische Universität Berlin, Hardenbergstr. 36, 10623 Berlin, Germany
[45]Astrobiology Center, 2-21-1 Osawa, Mitaka, Tokyo 181-8588, Japan
[46]JST, PRESTO, 2-21-1 Osawa, Mitaka, Tokyo 181-8588, Japan
[47]Department of Earth, Atmospheric and Planetary Sciences, MIT, 77 Massachusetts Avenue, Cambridge, MA 02139, USA
[48]Center for Astronomy and Astrophysics, TU Berlin, Hardenbergstr. 36, 10623 Berlin, Germany
[49]Institute of Geological Sciences, Freie Universität Berlin, Malteserstr. 74-100, 12249 Berlin, Germany
[50]Institute of Space Sciences (ICE, CSIC), Campus UAB, C/Can Magrans, s/n, 08193 Bellaterra, Spain
[51]Institut d'Estudis Espacials de Catalunya (IEEC), Barcelona, Spain

ABSTRACT

We report the discovery of an intermediate-mass transiting brown dwarf, TOI-503b, from the TESS mission. TOI-503b is the first brown dwarf discovered by TESS and orbits a metallic-line A-type star with a period of $P = 3.6772 \pm 0.0001$ days. The light curve from TESS indicates that TOI-503b transits its host star in a grazing manner, which limits the precision with which we measure the brown dwarf's radius ($R_b = 1.34^{+0.26}_{-0.15}\,\mathrm{R_J}$). We obtained high-resolution spectroscopic observations with the FIES, Ondřejov, PARAS, Tautenburg, and TRES spectrographs and measured the mass of TOI-503b to be $M_b = 53.7 \pm 1.2\,\mathrm{M_J}$. The host star has a mass of $M_\star = 1.80 \pm 0.06\,M_\odot$, a radius of $R_\star = 1.70 \pm 0.05\,R_\odot$, an effective temperature of $T_{\rm eff} = 7650 \pm 160$K, and a relatively high metallicity of 0.61 ± 0.07 dex. We used stellar isochrones to derive the age of the system to be ∼180 Myr, which places its age between that of RIK 72b (a ∼10 Myr old brown dwarf in the Upper Scorpius stellar association) and AD 3116b (a ∼600 Myr old brown dwarf in the Praesepe cluster). We argue that this brown dwarf formed in-situ, based on the young age of the system and the long circularization timescale for this brown dwarf around its host star. TOI-503b joins a growing number of known short-period, intermediate-mass brown dwarfs orbiting main sequence stars, and is the second such brown dwarf known to transit an A star, after HATS-70b. With the growth in the population in this regime, the driest region in the brown dwarf desert ($35 - 55 M_J \sin i$) is reforesting and its mass range shrinking.

Keywords: brown dwarfs – techniques: photometric – techniques: spectroscopic – techniques: radial velocities

1. INTRODUCTION

Brown dwarfs (BDs) are loosely defined as the objects that separate giant planets from low-mass stars. This definition is based on the mass of BDs, which ranges from $11 - 16\,\mathrm{M_J}$ (the approximate mass at which deuterium fusion can be sustained) to $75 - 80\,\mathrm{M_J}$ (the approximate mass to sustain hydrogen fusion) and yet, some of the most recent BD discoveries seem to blur these boundaries (Díaz et al. 2014; Zhou et al. 2019). The uncertainties in boundaries are caused by dependence on exact chemical composition of objects near these mass ranges Baraffe et al. (2002); Spiegel et al. (2011). One particular feature of the BD population is the apparent low occurrence rate of BDs in close orbits (i.e. within 3 AU) to stars in comparison to giant planets and stars. The apparent lack of short-period BDs is the so-called *brown dwarf desert* (e.g., Grether & Lineweaver 2006; Sahlmann et al. 2011). Although the population of BDs in this region has slowly grown in recent years (Csizmadia & CoRot Team 2016), the

gap remains significant. As every desert has a driest part, the driest part of the brown dwarf desert is the mass range between $35 \leq M_J \sin i \leq 55$ for orbital periods under 100 days (Ma & Ge 2014a). Some authors use the existence of this gap to motivate the idea that there are two separate BD populations that result from two different BD formation processes. In this case, the two processes are formation via core accretion in a protoplanetary disk (the way giant planets are thought to form) and formation by gravitational instability, which is how stars are thought to typically form. For the transiting BD population, this gap appears at a mass centered around 42.5 M_J (Ma & Ge 2014a). Different studies suggest suppressing the distinction between BDs and the coolest M stars given their similarities (Whitworth 2018), while others suggest that BDs and giant planets form a continuum based on their mass-density relation (Hatzes & Rauer 2015; Persson et al. 2019), which, in turn, implies that the range of giant planets spans 0.3-60 M_J or 0.3-73 M_J, respectively. Given this variety of interpretations of what separates giant planets, BDs, and low-mass stars, each new, well-characterized BD system, especially the ones that reside in the driest part of the brown dwarf desert, will be important to understanding this population as a whole.

We search for transiting BDs in particular because of the extra information that is obtained from a transiting object. In many cases, given the reliability of our stellar models, we may precisely (i.e. on the order of a few percent) measure the radius and mass of a transiting or eclipsing companion. These two properties are fundamental to an object's physical behavior and evolution. This value is enhanced for transiting BDs given that they are so uncommon and that the substellar evolutionary models that aspire to describe these objects stand to be more rigorously tested with a larger sample that has well-characterized masses and radii. With only a minimum mass provided by a radial velocity (RV) orbit, we cannot verify if a companion is truly a BD or something more massive, like a star. With only a radius that is derived from stellar models and a light curve, we cannot determine if the stellar companion is a giant planet, a BD, a low-mass star, some form of stellar activity, or a false-positive. Only with RVs and photometry combined may we identify BDs and test the mass-radius predictions of substellar evolutionary models.

This is where space-based photometric survey missions are particularly useful and often one of the best options for characterization of short-period transiting BDs. This was the case for the CoRoT mission (Rouan et al. 1998) and the *Kepler/K2* missions (Borucki et al. 2010), which made enormous contribution to exoplanetary science. So far, we are seeing the similar impact from the Transiting Exoplanet Survey Satellite (TESS[1]) mission (Ricker et al. 2015) and we expect this impact to grow not only in the realm of small exoplanets, but for the transiting BD population as well. One aspect of TESS that distinguishes it from CoRoT and *Kepler/K2* is the number of bright stars it will observe. This makes potential BD host stars more accessible to spectroscopic facilities that may be used in coordination with TESS as well as the *Gaia* mission (for precise parallaxes) to detect and characterize BDs. The endeavor to discover more BDs is aided further by the relatively deep transit depths of BDs around typical main sequence stars and the relatively large semi-amplitude signals relevant to RV follow-up. In total, there are more than 2,000 known BDs (e.g., Skrzypek et al. 2016), with approximately 400 of these in bound systems. Of these, only 21 transit their host stars (with an additional 2 in a BD binary), which makes a nearly all-sky transit survey mission like TESS an important tool in expanding and exploring the transiting BD population.

In this paper, we report the discovery of TOI-503b, the first BD known to orbit a metallic-lined A star (Am star). Based on the age of 180 Myr that we derive from stellar isochrones and the circular orbital solution for the companion BD, we argue that this particular BD formed in-situ. This work is the result of a collaboration between the KESPRINT consortium (e.g., Hjorth et al. 2019; Korth et al. 2019; Livingston et al. 2019; Palle et al. 2019; Gandolfi et al. 2019; Persson et al. 2019), PARAS-PRL India (Chakraborty et al. 2014), and the Harvard-Smithsonian Center for Astrophysics. We describe the observations in Section 2, the data analysis in Section 3 and provide a final discussion in Section 4.

2. OBSERVATIONS

2.1. *TESS light curves*

TESS monitored TOI-503 at a two-minute cadence from January 8 to February 1, 2019 (∼24.5 days). There is a gap of 1.7 days during this time due to the transfer of data from the spacecraft. The TESS Input Catalog (TIC) ID of the source is 186812530 (Stassun et al. 2018b) and it was observed in CCD 3 of camera 1 in Sector 7. TOI-503 will not be observed in any upcoming sectors of the primary TESS mission. We use the publicly available Pre-search Data Conditioning Simple Aperture Photometry (PDCSAP) light curves at Mikulski Archive for Space Telescopes (MAST)[2] that are pro-

[1] https://heasarc.gsfc.nasa.gov/docs/tess/

[2] https://mast.stsci.edu/portal/Mashup/Clients/Mast/Portal.html

Table 1. Basic parameters for TOI-503

Parameter	Description	Value	Source
α_{J2000} ...	Right Ascension (RA).....	08 17 16.89	1
δ_{J2000}	Declination (Dec).....	12 36 04.76	1
T	TESS T mag.....	9.187 ± 0.018	2
G	Gaia G mag.....	9.350 ± 0.002	1
B_T	Tycho B_T mag.....	9.703 ± 0.026	3
V_T	Tycho V_T mag.....	9.428 ± 0.024	3
J	2MASS J mag.....	8.945 ± 0.023	4
H	2MASS H mag.....	8.935 ± 0.017	4
K_S	2MASS K_S mag.....	8.895 ± 0.016	4
WISE1...	WISE1 mag.....	8.868 ± 0.023	5
WISE2...	WISE2 mag.....	8.885 ± 0.020	5
WISE3...	WISE3 mag.....	8.888 ± 0.029	5
WISE4...	WISE4 mag.....	8.558 ± 0.020	5
μ_δ	PM in RA (mas/yr).....	-9.336 ± 0.095	1
μ_δ	PM in DEC (mas/yr).....	-9.945 ± 0.053	1
π	Parallax (mas).....	3.887 ± 0.059	1
RV.....	Systemic RV (km/s).....	29.469 ± 0.013	6

Other identifiers:

TIC 186812530
TYC 802-751-1
2MASS J08171689-1236049
Gaia DR2 650254479499119232

NOTE—References: 1 - Lindegren et al. (2018), 2 - Stassun et al. (2018b), 3 - Høg et al. (2000), 4 - Cutri et al. (2003), 5 - Cutri & et al. (2013), 6 - this work

vided by the TESS Science Processing Operations Center (SPOC). The PDCSAP light curves have the systematics of the spacecraft removed. The SPOC pipeline (Jenkins et al. 2016) was used to extract the light curve and associated uncertainties from the original scientific data. We normalize this light curve by dividing it by the median-smoothed flux, which can be seen in Figure 1. A total of 6 transits spaced at a period of ∼3.7 days are visible with depths of ∼4500 ppm. The TESS data validation reports (Jenkins et al. 2016) identify TOI-503 as the host of a planet candidate with an estimated radius of $1.13 \pm 0.28\,R_J$ by fitting the TESS light curve and using host star parameters from Stassun et al. (2019). The basic parameters of the star are listed in Table 1.

2.2. *Ground-based light curves*

As part of the TESS Follow-up Observation Program (TFOP) additional ground-based photometry was carried out by the Sinistro camera on the Las Cumbres Observatory (LCO), Siding Spring Observatory (SSO) 1.0-m, the Santa Barbara Instrument Group (SBIG) camera on the LCO 0.4-m, the Chilean Hungarian Automated Telescope (CHAT) 0.7-m telescope, and the *KeplerCam* instrument on the Fred Lawrence Whipple Observatory (FLWO) 1.2-m telescope. The LCO-SSO observations were taken in the Y-band and confirmed that there are no nearby or background eclipsing binaries within 2′.5 that were blended in the aperture of camera 1 from TESS. The transit was not detected by LCO-SSO due to the insufficient amount of out-of-transit baseline flux. The observations with SBIG show a clear ingress, but do not extend long enough to show the egress of the transit due to the target star reaching a high airmass. A full on-time transit was detected by CHAT in the i' band as well as the *KeplerCam* instrument in the z band. Both of these were very shallow, but on-time detections, confirming the ephemeris from TESS. We decide against incorporating any ground-based follow-up in our analysis due to the shallow nature of this transit and the low transit depth signal-to-noise ratio.

2.3. *Contamination from nearby sources*

The TFOP was also responsible for observations of TOI-503 with Gemini/NIRI on March 22, 2019 and again with Keck/NIRC2 (Wizinowich et al. 2000) on April 7, 2019 (Figure 2). In each case, observations were taken in NGS mode in the Br-γ filter with the target as the guide star. Images were dithered, such that a sky background could be constructed, with a square dithering pattern for the NIRI data and a 3-point pattern for the NIRC2 data to avoid the known noisy fourth quadrant. For each instrument we used the same basic reduction procedure: images were flat-fielded and sky-subtracted, and the dithered frames aligned and co-added.

Sensitivity was determined by injecting simulated sources azimuthally around the primary target, at separations of integer multiples of the central source's full width at half maximum (Furlan et al. 2017). The brightness of each injected source was scaled until standard aperture photometry detected it with 5σ significance. The resulting brightness of the injected sources relative to the target set the contrast limits at that injection location. The final 5σ limit at each separation was determined from the average of all of the determined limits at that separation and the uncertainty on the limit was set by the rms dispersion of the azimuthal slices at a given radial distance. No nearby contaminating sources are identified in either image, and at $1''$ we reach contrasts of Δmag=8.0mag in the NIRI data and Δmag=7.2mag in the NIRC2 data.

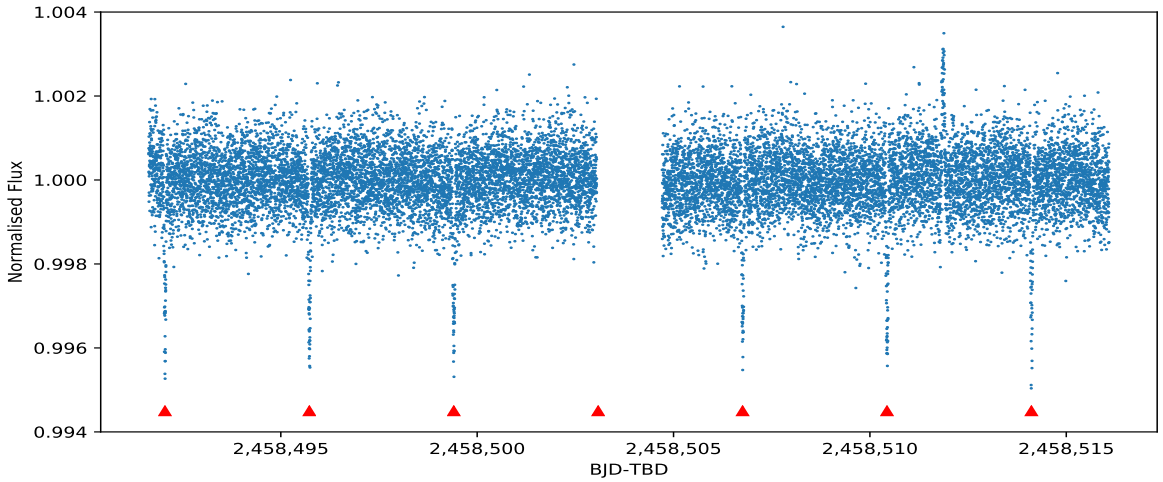

Figure 1. The normalized light curve of TOI-503 observed by TESS is plotted in blue with red triangles denoting the time of each transit. Six transits can be seen spaced every ∼3.7 days with a depth of ∼4500 ppm.

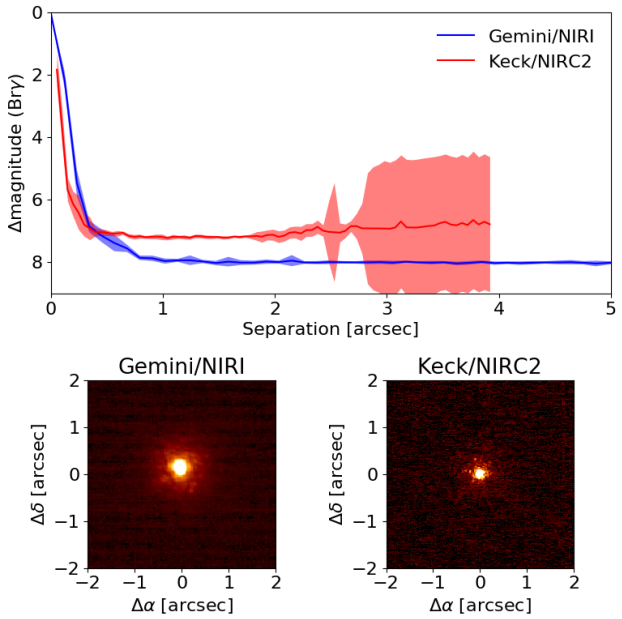

Figure 2. Sensitivity curve as a function of angular separation for TOI-503 from Gemini/NIRI and Keck/NIRC2. The inset shows the image of the target star from each instrument.

2.4. *KESPRINT spectra*

We obtained a total of 50 spectra of TOI-503 between March 18, 2019 and April 17, 2019 using KESPRINT observing time on the 2-m Perek telescope at the Ondřejov Observatory, the 2-m Alfred Jensch telescope at Tautenburg, and the 2.56-m Nordic Optical Telescope (NOT) at the Roque de Los Muchachos Observatory. Using the central Europe monitoring network with telescopes in Ondřejov and Tautenburg for simultaneous observations has the advantage to allow a better coverage of observing data. Furthermore, both telescopes are capable of long term monitoring of interesting objects (Kabáth et al. 2019b). For these reasons, such observations are often performed (Skarka et al. 2019; Kabáth et al. 2019a; Sabotta et al. 2019). RVs from all used telescopes beyond the KESPRINT are reported in Table 2.

2.4.1. *Ondřejov spectra*

We collected a set of 14 spectra using the Ondřejov Echelle Spectrograph, which has a spectral resolving power R ≈ 44 000 over the wavelength range of 370nm to 850nm (Kabáth et al. 2019b). All spectra have an exposure time of 3600 s resulting in a signal-to-noise (S/N) per pixel at 550nm varying between 16–22, depending on the observing conditions and the airmass. We use the standard IRAF 2.16 routines (Tody 1993) to process the spectra, which were corrected for bias, flat field and cosmic rays. The spectrum with the highest S/N was used as template for the cross-correlation done with the IRAF `fxcor` routine, allowing us to remove instrumental shift by measuring the shift in telluric lines, and to measure the relative RVs. The errors are standard deviations of values from eighteen 10nm intervals that were considered.

2.4.2. *FIES spectra*

We acquired 8 spectra with the FIbre-fed Échelle Spectrograph (FIES; Frandsen & Lindberg 1999; Telting et al. 2014) mounted at the 2.56-m Nordic Optical Telescope (NOT) of Roque de los Muchachos Observatory (La Palma, Spain). FIES has a resolving power of R ≈ 47 000. The observations were carried out between March 21 and April 15, 2019 UT, as part of the observing

programs 58-024 and 59-210. The exposure time was set to 1500–2100 s – depending on sky and seeing conditions –, leading to a S/N ratio per pixel of ∼70-100 at 5500 Å. We followed the observing strategy described in Buchhave et al. (2010) and Gandolfi et al. (2015) and traced the RV drift of the instrument by acquiring long-exposed ThAr spectra ($T_{\rm exp} \approx 60$ s) immediately before and after each science exposure. We reduced the FIES spectra following standard IRAF and IDL routines and extracted the RV measurements via multi-order cross-correlations with the RV standard star HD 182572 (Udry et al. 1999) observed with the same instrument set-up as TOI-503.

2.4.3. *Tautenburg spectra and Doppler Tomography analysis*

We used the 2-m Alfred Jensch telescope of the Thüringer Landessternwarte Tautenburg to obtain 28 spectra. The telescope is equipped with an echelle spectrograph with spectral resolving power R ≈ 35 000 with the 2″ slit used. The spectra used for orbital analysis have an exposure time 1200 s resulting in an S/N ratio between 23 and 27. We processed the spectra using the Tautenburg Spectroscopy pipeline (Sabotta et al. 2019) built upon PyRaf and the Cosmic Ray code by Malte Tewes based on the method by van Dokkum (2001). We use cross-correlation routines from IRAF to correct spectra for the shift in telluric lines and to measure the relative RVs. There are 17 spectra from the 28 which have an exposure time of 600 s and that were taken in an attempt to extract a Doppler tomography (DT) (e.g., Hatzes 1998; Albrecht et al. 2007; Collier Cameron et al. 2010a) signal during the transit night of April 17, 2019. These are not used for the RV measurements to avoid the signal created by the BD blocking light from the host star, which creates an additional Doppler shift that is based on the orbital alignment and rotation rate of the star and not the orbital motion of the BD.

The DT technique reveals the distortion of the stellar line profiles when a planet or BD blocks part of the stellar photosphere during a transit. This distortion is a tiny dip in the stellar absorption profile, scaled down in width according to the BD-to-star radius ratio. Additionally, the area of that dip corresponds to the BD-to-stellar disks area ratio. As the BD moves across the stellar disk, the dip produces a trace in the time series of line profiles, which reveals the spin-orbit alignment between the star and BD orbit. For this analysis, we first created a reference stellar absorption spectrum consisting of delta functions at the wavelength positions of the observed stellar absorption lines. Their positions and strengths were determined by fitting each stellar absorption line in the observed spectrum with the rotational profile of TOI-503 ($v \sin i = 26 \mathrm{kms}^{-1}$). A total of 410 stellar absorption lines were identified in the wavelength range from 455.8 to 674.6nm. We excluded those wavelength regions from our analysis which exhibited telluric lines, the Hydrogen Balmer absorption lines and the Na II doublet around 589nm.

By employing a least-squares deconvolution similar to what is shown in Collier Cameron et al. (2002) of the observed spectra with the reference spectrum, we summed up the 410 stellar absorption lines in each spectrum into one high S/N mean line profile. The resulting line profiles were scaled so that their height was one, and were interpolated onto a velocity grid of 2.65 km/s increments, corresponding to the velocity range of one spectral pixel at 550nm. We then summed up all the mean line profiles collected the nights before the transit and subtracted the resulting profile from the in-transit ones. Figure 3 shows the residuals of the line profiles and shows that we are unable to detect a trace of the transiting planet using this method. The non-detection of the shadow of the planet confirms that the object is grazing which is in agreement with the impact parameter derived from transit light curve.

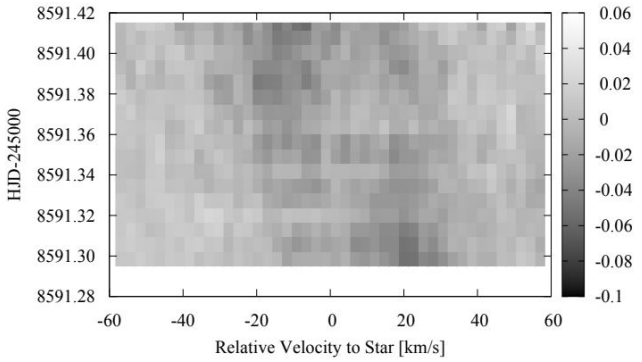

Figure 3. Doppler tomography using Tautenburg in-transit spectra.

2.5. *TRES spectra*

We used the Tillinghast Reflector Echelle Spectrograph (TRES) on Mt. Hopkins, Arizona to obtain spectra of TOI-503 between March 23 and April 14, 2019. The spectrograph has a resolving power of R ≈ 44 000 and covers wavelengths from 390nm to 910nm. Forty-three spectra of TOI-503 were taken with TRES with exposure times ranging from 195–300 s and S/N ranging from 35 to 59. The relative RVs that we derive from TRES spectra use multiple echelle orders from each spectrum that are cross-correlated with the highest S/N spectrum of the target star. We omit individual orders with poor S/N and manually remove obvious cosmic rays. Of these 43 spectra, 33 were taken in an attempt

Table 2. Multi-order relative radial velocities of TOI-503 from Ondřejov, FIES, Tautenburg, TRES, and PARAS.

$BJD_{TDB} - 2450000$	RV (m/s)	σ_{RV} (m/s)	Instrument
8566.651866	-24.9	84.6	TRES
8568.628445	8720.4	87.6	TRES
8569.654306	1721.4	76.6	TRES
8570.631553	1140.6	35.6	TRES
8571.619256	8129.6	52.7	TRES
8572.647920	6927.5	71.7	TRES
8573.712391	30.2	54.1	TRES
8574.660766	3615.3	65.4	TRES
8575.644821	9286.9	51.2	TRES
8576.674889	4227.1	59.9	TRES
8577.649209	-64.4	47.5	TRES
8587.709792	4140.1	63.7	TRES
8581.233706	-4877.9	92.1	PARAS
8582.207307	539.1	70.9	PARAS
8582.238727	805.1	88.6	PARAS
8583.212860	4393.9	85.7	PARAS
8583.242544	4175.4	100.8	PARAS
8584.201377	-1800.3	86.5	PARAS
8585.220041	-3730.9	87.4	PARAS
8564.408181	7370.8	250.5	ONDŘEJOV
8564.450341	7663.6	191.3	ONDŘEJOV
8565.411871	5208.5	292.7	ONDŘEJOV
8565.454031	4899.8	452.4	ONDŘEJOV
8566.414342	-1016.0	405.8	ONDŘEJOV
8572.314192	7360.1	391.9	ONDŘEJOV
8575.276802	6639.4	291.2	ONDŘEJOV
8575.369402	7511.8	227.1	ONDŘEJOV
8575.419602	7484.1	305.0	ONDŘEJOV
8578.300872	2048.7	274.6	ONDŘEJOV
8578.343032	2911.4	199.8	ONDŘEJOV
8578.385192	3016.4	222.3	ONDŘEJOV
8581.353282	-674.9	427.5	ONDŘEJOV
8581.395442	-829.4	409.7	ONDŘEJOV
8559.414221	-7002.3	212.0	TAUTENBURG
8561.366911	1000.0	80.0	TAUTENBURG
8562.458981	-6541.5	200.3	TAUTENBURG
8563.348001	-5693.6	143.8	TAUTENBURG
8567.360682	-3341.8	128.5	TAUTENBURG
8589.311442	-4202.8	160.8	TAUTENBURG
8589.326082	-3905.7	160.8	TAUTENBURG
8589.340732	-4058.3	82.7	TAUTENBURG
8590.312772	1848.7	200.9	TAUTENBURG
8590.326992	1853.5	185.5	TAUTENBURG
8590.341222	1665.8	273.4	TAUTENBURG
8564.442588	33708.6	26.8	FIES
8566.400806	24939.9	33.5	FIES
8581.364308	24956.5	36.1	FIES
8583.434302	33152.1	32.4	FIES
8587.367559	31681.2	21.5	FIES
8587.474228	30949.2	27.0	FIES
8588.453630	24951.0	45.7	FIES
8589.369006	28516.5	47.5	FIES

to extract a DT signal, but as with our analysis of the Tautenburg in-transit DT spectra, we do not find a noticeable signal, which confirms the grazing nature of the BD transit.

2.6. *PARAS spectra*

We obtained 7 spectra with the PARAS spectrograph (Chakraborty et al. 2014) coupled with the 1.2-m telescope at Gurushikhar Observatory, Mount Abu, India between April 6 to April 11, 2019 at a resolving power of $R \approx 67\,000$, in the wavelength range of 380nm to 690nm. Each night had a median seeing of around 1.5″. The exposure time for each measurement was kept at 1800 s, which resulted in a S/N of 20–25 at the blaze peak wavelength of 550nm. The spectra were extracted using a custom-designed automated pipeline written in IDL, based on the algorithms of Piskunov & Valenti (2002). The extracted spectra were cross-correlated with the template spectrum of an A-type star to calculate the relative RVs. Further details of the spectrograph and data analysis procedure can be found in Chakraborty et al. (2014). The uncertainties reported here are the cross-correlation function fitting errors combined with the photon noise in the same way as described in Chaturvedi et al. (2016, 2018).

3. ANALYSIS

3.1. *Modeling Stellar Parameters*

We use `iSpec` (Blanco-Cuaresma et al. 2014; Blanco-Cuaresma 2019) and the Stellar Parameter Classification (`SPC`) software Buchhave et al. (2012) to analyze the spectra of TOI-503. Then, with the spectral properties as well as an SED, light curve, and *Gaia* parallax of the star, we use `EXOFASTv2`, and combination of `PARAM 1.3` (to model the stellar parameters) (da Silva et al. 2006), `GeePea` (to model the light curve) (Gibson et al. 2012) and `Systemic Console 2` (to model the RV curve) (Meschiari et al. 2009) to independently model the star and BD.

3.1.1. `iSpec` *Stellar Parameters*

We use `iSpec` to perform a detailed analysis of the host star from the FIES spectra. Specifically, we use the Synthe radiative transfer code (Kurucz 1993), the MARCS atmosphere models (Gustafsson et al. 2008), and version 5 of the GES atomic line list (Heiter et al. 2015) between 420 and 920nm, which includes 35 different chemical species. These are incorporated into the framework of `iSpec`. We co-add all the 8 FIES spectra (after the RV shift correction) to increase the S/N and use them to determine the effective temperature $T_{\rm eff}$, metallicity [Fe/H], surface gravity $\log g$, and the projected stellar equatorial velocity $v \sin i$. We model the

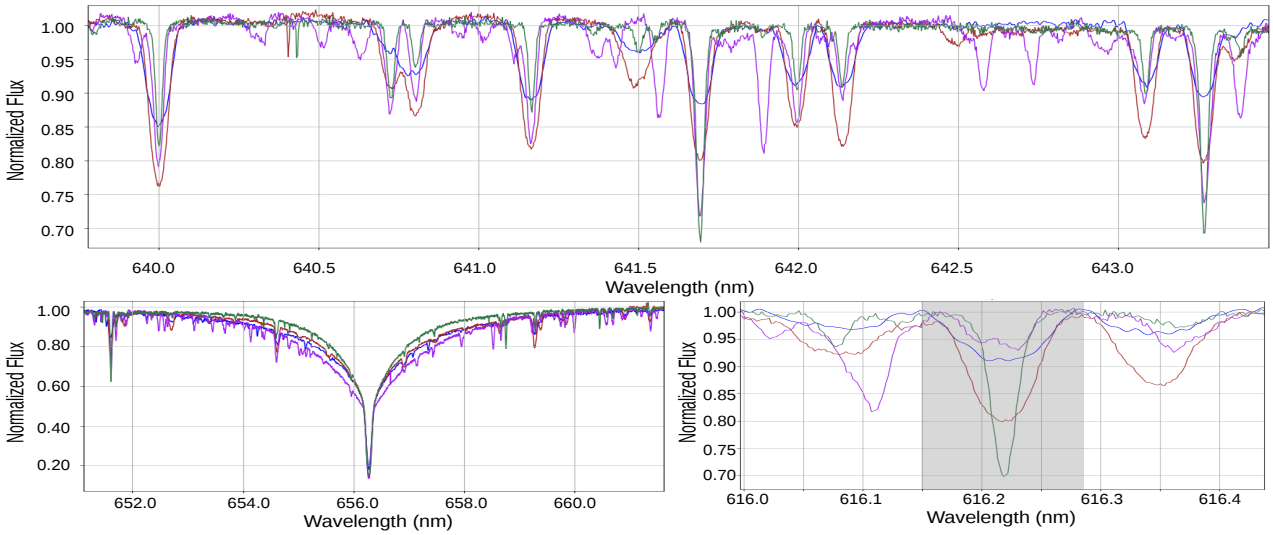

Figure 4. Spectrum of TOI-503 (blue line) and three templates with similar temperatures (A-star template – green line, Am-star template – orange line, Ap-star template – purple line), over-plotted for comparison. Top: iron lines region. Bottom left: the Hα Balmer line. Bottom right: a CaI line.

stellar parameters using the Bayesian parameter estimation code `PARAM 1.3` and use the parallax measured by *Gaia* DR2 ($\varpi = 3.8875 \pm 0.0591$ mas; Lindegren et al. 2018) for the distance of the star. `PARAM 1.3` code estimates stellar properties using the PARSEC isochrones (Bressan et al. 2012). We calculate the value of $\log g$ iteratively to ensure an agreement between `iSpec` and `PARAM 1.3`. We determine the effective temperature by fitting the Hα Balmer line (Cayrel et al. 2011), and the metallicity by fitting for 22 Fe I lines in the interval 597nm to 643nm. From this analysis, we find TOI-503 to be a metallic-line A star, or Am star, with a metallicity of $[\mathrm{Fe/H}] = 0.61 \pm 0.07$.

The formation of Am stars is generally attributed to the slowing of the stellar rotation via tidal force caused by a binary star (Michaud et al. 1983). Am stars are generally slow rotators compared to typical A stars, with rotation rates below 120 km/s (Abt & Morrell 1995). The study by Abt & Moyd (1973) suggests that all slowly rotating A-type main sequence stars are chemically peculiar, i.e. those with high iron abundance or unusual an depletion of key elements such as Ca. The rotation period of TOI-503 ($P_{\mathrm{rot}} = 3.64$ days) is determined from the projected stellar equatorial velocity, the inclination derived from `GeePea` and the radius of the star derived from `PARAM 1.3`. The rotation period of the star is similar to the orbital period of the BD ($P_{\mathrm{orb}} = 3.67$ days), which is indicative of synchronism. Such a slow rotation rate would enable the onset of radiative diffusion within the stable atmosphere, which leads to the abundance of elements observed in the spectrum, as in Am stars (Michaud et al. 1983). In this context, comparing the TOI-503 spectrum with the templates of a normal A-type star, a magnetically peculiar Ap star, and an Am star from the ESO database[3] reveals the clear similarity between the observed spectrum of TOI-503 and that of the Am stars (Figure 4). However, the most persuasive argument would be that the overabundance (in context of A-type stars) of the iron group elements is coupled with an underabundance of key light elements, such as Ca, Sc, or Mg, which is the characteristic sign of Am stars. The abundances we derive point exactly to this conclusion, thereby confirming the Am classification. The stellar parameters and the abundances of selected species are reported in Table 3.

3.1.2. *Stellar Parameter Classification and* `EXOFASTv2` *modeling*

We also use `SPC` with the TRES spectra to independently (from `iSpec` and FIES) derive effective temperature (T_{eff}), metallicity ([Fe/H]), surface gravity ($\log g$), and the projected stellar equatorial velocity ($v \sin i$) for TOI-503. We iteratively use `SPC` with `EXOFASTv2` (Eastman et al. 2019) to determine values for T_{eff} and [Fe/H], meaning that we use the $\log g$ from `EXOFASTv2` as a fixed parameter in `SPC` and then take the T_{eff} and [Fe/H] from `SPC` (with the fixed $\log g$ from `EXOFASTv2`) as starting values in a new `EXOFASTv2` analysis. However, due to the upper limit of $[\mathrm{Fe/H}] \leq +0.5$ for the metallicity of the MIST isochrones (Dotter 2016; Choi et al. 2016; Paxton et al. 2015) that `EXOFASTv2` utilizes, we rely on

[3] http://www.eso.org/sci/observing/tools/uvespop/field_stars_uptonow.html

our measurements using iSpec for the metallicity. With SPC, we measure a metallicity of [Fe/H] = 0.34 ± 0.08 with a fixed $\log g = 4.23$ from an initial EXOFASTv2 analysis. The parameters $T_{\rm eff}$, [Fe/H], and $\log g$ are not fixed in subsequent EXOFASTv2 analyses and only $\log g$ is fixed in subsequent SPC anaylses. The [Fe/H] value is about 0.27 dex lower than our value from iSpec most likely because SPC explicitly measures [m/H], which is a good approximation for [Fe/H] assuming a Solar-like composition and chemical proportions (not the case for TOI-503). We use SPC on a co-added spectrum with the RV shifts corrected for. We do not co-add any spectrum with S/N<15. With SPC, we use the 503-532nm wavelength range (centered on the Mg b triplet) on a single co-added TRES spectrum.

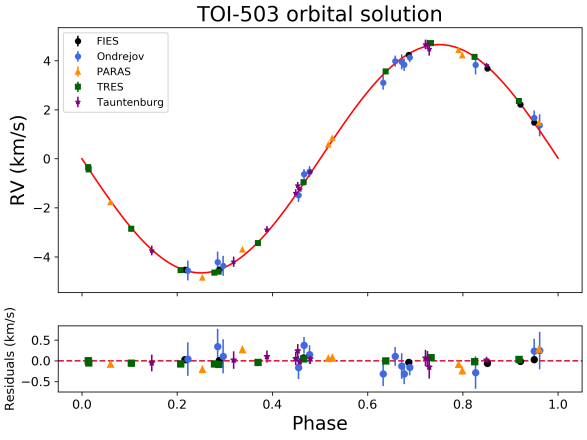

Figure 5. Orbital solution for TOI-503 showing the EXOFASTv2 RV model in red. This orbital solution is jointly derived by simultaneously fitting all RVs from the different contributing spectrographs and the normalized PDCSAP TESS light curve.

We derive the mass and radius of the BD using EXOFASTv2, which uses the Monte Carlo-Markov Chain (MCMC) method. For each MCMC fit, we use N=36 (N = $2\times n_{\rm parameters}$) walkers, or chains, and run for 50,000 steps, or links. We modeled the host star mass and radius using the MIST isochrones, which are integrated into the framework of EXOFASTv2. Figure 5 shows the orbital solution we derive with EXOFASTv2 with a joint fit of the RV and transit data. Our transit solution from this same joint fit agrees with that shown via the GeePea analysis (Figure 7). We account for interstellar extinction, A_V, using the Galactic dust and reddening extinction tool from IRAS and COBE/DIRBE [4] and take this value of $A_V = 0.0791$ as an upper limit for our priors in EXOFASTv2. We also use the parallax of TOI-503 as measured by *Gaia* DR2 and the SPC results for $T_{\rm eff}$ and metallicity ([Fe/H] = 0.34) as starting points for our priors. The full list of free parameters we specify for each object is: period P, time of conjunction (T_C in BJD), host star effective temperature $T_{\rm eff}$, host star metallicity [Fe/H], RV semi-amplitude K, RV relative offset to the systemic velocity γ_{rel}, interstellar extinction A_V, parallax, orbital inclination i, and $R_B/R_\star$. We initially allow the eccentricity e to be a free parameter and find it to be close to zero at $e \approx 0.005 \pm 0.002$. In order to avoid the Lucy-Sweeney bias (Lucy & Sweeney 1971), we fix the eccentricity to zero in all subsequent analyses. The derived $T_{\rm eff}$ from EXOFASTv2 agrees well with the spectroscopic $T_{\rm eff}$ from SPC. We impose Gaussian priors on these free parameters in EXOFASTv2. The median value with 1-σ uncertainties of the MCMC chains for each parameter is reported in Table 6. The parameters derived from EXOFASTv2 are consistent with those derived from our other independent analyses.

[4] Galactic dust and reddening extinction tool: https://irsa.ipac.caltech.edu/applications/DUST/

Table 3. Comparison of parameters between analysis methods. The parameters here are the median values except for the EXOFASTv2 R_p, which shows both the median and the mode.

Parameter	SPC & EXOFASTv2	iSpec/PARAM 1.3 & GeePea/Systemic Console 2
M_b (M_J)	53.7 ± 1.2	53.6 ± 1.1
R_b (R_J)	1.34 ± 0.26	1.29 ± 0.30
$R_{b,\rm mode}$ (R_J)	1.27 ± 0.15	–
Period (days)	3.6772 ± 0.0001	3.6775 ± 0.0002
a/R_*	7.22 ± 0.22	7.47 ± 0.19
R_b/R_*	0.0805 ± 0.015	0.0724 ± 0.015
b	0.974 ± 0.022	0.956 ± 0.023
Inclination i (degree)	82.25 ± 0.41	82.65 ± 0.38
e	0 (adopted)	0 (adopted)
$M_\star$ ($M_\odot$)	1.80 ± 0.06	1.80 ± 0.02
$R_\star$ ($R_\odot$)	1.70 ± 0.05	1.79 ± 0.04
$\log g$	4.23 ± 0.03	4.16 ± 0.24
$T_{\rm eff}$ (K)	7650 ± 160	7639 ± 105
[Fe/H]	0.30 ± 0.09	0.61 ± 0.07
[Ni/H]	–	0.58 ± 0.09
[Ca/H]	–	-0.40 ± 0.11
[Sc/H]	–	0.10 ± 0.14
[Mg/H]	–	0.25 ± 0.15
$v_{\rm rot} \sin i_\star$ (km/s)	28.6 ± 0.4	25.0 ± 0.3
$P_{\rm rot}$ (days)	3.01 ± 0.09	3.64 ± 0.13

3.1.3. *Analysing the surface rotation*

Even though it is not completely clear that A-type stars have spots, there are a variety of studies on the

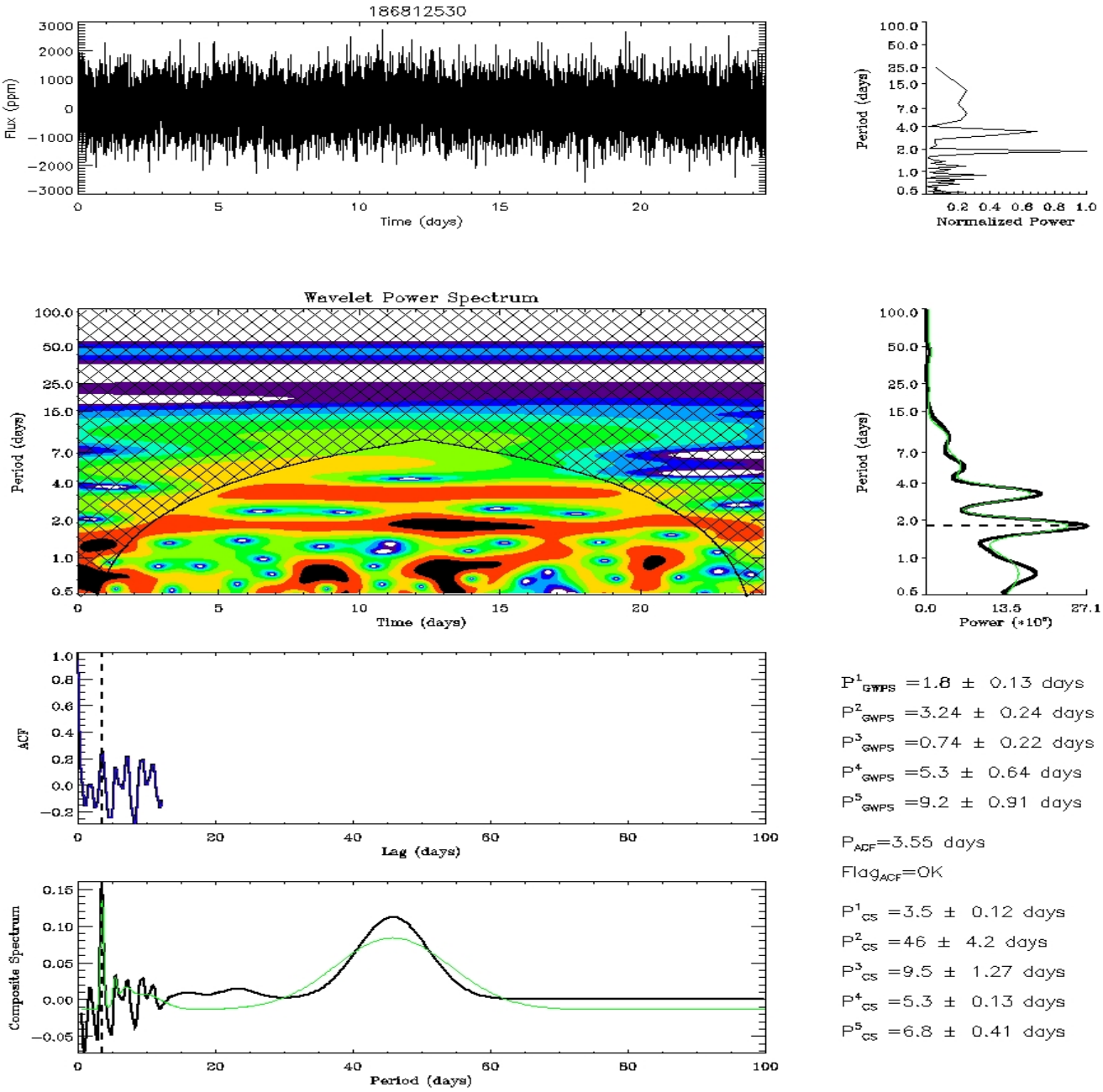

Figure 6. The analysis of modulations in light curve of TOI-503. Description of the images from top to bottom: First: The light curve cleared for primary and secondary transits. Second: Wavelet power spectrum of the light curve with GWPS (black) and corresponding Gaussian fit (green) next to it. Third: ACF of the light curve Fourth: CS of the light curve (black) with corresponding Gaussian fit (green).

discovery of spots on the well-known star, Vega (Böhm et al. 2015; Petit et al. 2017; Balona 2017) and more studies about the measurement of the rotation based on spot modulation for A-type stars (Balona 2011, 2013). There is even previous evidence of the detectable presence of spots on Am-type stars (Balona et al. 2015). So, it is reasonable to search for the signature of the rotation period through the modulation caused by the star spots in TOI-503. To do this, we use the SPOC two-minute cadence light curve of TOI-503. We removed the signal of the primary and secondary transits using the known ephemerides and then fill all gaps using inpainting techniques based on a multi-scale cosine trans-

form as described in García et al. (2014a) and Mathur et al. (2014).

We then search for modulation in the resulting light curve by performing the following steps. First, we perform a time-frequency analysis based on wavelets decomposition (Torrence & Compo 1998; Mathur et al. 2010; García et al. 2014b) to compute the wavelet power spectrum (WPS), which we subsequently project on the period axis to form the global wavelets power spectrum (GWPS). In the second step, we perform autocorrelation function analysis (ACF, McQuillan et al. 2014) to extract the most significant signal, which corresponds to a particular period. Finally, by a combination of previous two steps (specifically multiplying them), we create a function called the Composite Spectrum (CS) (Ceillier et al. 2016, 2017). As these steps are sensitive to different types of artifacts in a light curve, by deriving the CS, we can mask such artifacts and highlight a periodic signal created by stellar activity such as star spots. The pipeline that combines these different techniques has been applied to simulated data (Aigrain et al. 2015) and has been already performed to a large number of solar-like stars and red giants (e.g. Santos et al. 2019) with reliable success.

The original light curve analysis with the transits provides a period of $P_{GWPS} = 3.66$ days, corresponding to the orbital period of the BD. Once the transits are removed, we find a period of $P_{GWPS} = 3.24$ days with the wavelet analysis and $P_{ACF} = 3.55$ days with the ACF analysis. The height of the peak in the ACF (H_{ACF}, measured from the maximum to the adjacent minima) is 0.5, which fulfills our criteria for a reliable result ($H_{ACF>0.4}$). We note that we detect the overtone of half of the real rotation period $P_{GWPS} = 1.8$ days using wavelets decomposition analysis, which can be seen in Figure 6. This period is detected in power spectra quite often and happens when we observe active regions on the visible side of the star and diametrically opposite side of the star. This period is absent in the CS power spectrum and reveals the final period of $P_{CS} = 3.50 \pm 0.12$ days. These results are slightly lower than the BD orbital period, but still quite close to it. The rotation period found (Table 3) also agrees with the values obtained spectroscopically from the `iSpec` and `SPC` analyses. However, given the close values of the rotation period with the orbital period, we cannot completely rule out that the modulation we measure is affected by the orbital motion of the BD.

3.1.4. *Transit light curve fitting with* `GeePea`

TOI-503 has a V-shaped, grazing transit. In general, V-shaped eclipses are are often considered false positives caused by binary stars with similar radii, stellar grazing eclipses, or a blended eclipsing binary, such as a background binary or one bound to the target star in a triple system. In this case, we ruled out the possibility of a false positive scenario with a combination of follow-up RVs to determine the mass of the companion, high-resolution imaging to rule out a blend, and ground-based follow-up photometry from the TFOP. This implies a rather low inclination in context of BDs that we measure to be roughly $i = 82.25° \pm 0.41$ or an impact parameter of $b = 0.974^{+0.022}_{-0.015}$. There are slightly more than 10 similar systems known (Alsubai et al. 2018), but only one that includes a BD (Csizmadia et al. 2015a). The analysis of grazing eclipses is rather challenging and often degenerate between the radius of the transiting object and its impact parameter b.

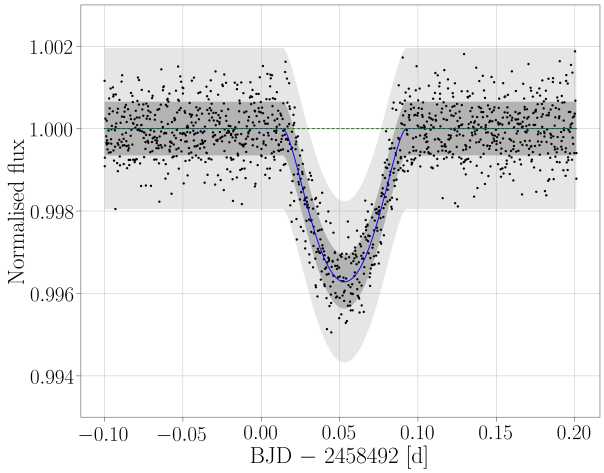

Figure 7. The transit light curve of the TOI-503, fitted with the GP model described in Sect. 3.1.4. The blue line represents the best fitting transit light curve and the green line shows the model without the transit function. The dark and light grey regions represent the 1-σ and 3-σ prediction of the GP model.

We fit the light curve using the `GeePea` code, which is based on Gaussian Processes (GPs) and described by Gibson et al. (2012). We use square exponential kernel function and assume uniform, uninformative priors for all the parameters with the exception of the limb darkening coefficients, chosen so as to ensure a positive surface brightness. All hyper-parameters of the noise model are chosen such as to ensure they are positive. Since limb darkening, radius ratio, and impact parameter are degenerate here due to the grazing transit geometry, the fitted values for the radius ratio and impact parameter dominate the limb darkening measurement. Considering this, we set Gaussian priors on the limb darkening coefficients obtained from the tables of Claret (2017). The

fit of the light curve is presented in Figure 7. We use the MCMC method with four chains with 1,000 walkers of 40,000 iterations to find out the uncertainties for the free parameters of the transit and noise model. Plots of posterior distributions and correlation plots are presented in Figure 12. The determined values for the parameters are summarized in Table 3 and are found independently from those found using `EXOFASTv2`.

We also use other analysis tools to perform independent analyses of the RV and transit data and derive the stellar and the BD parameters of TOI-503: `PYANETI` (Barragán et al. 2019) and `MISTTBORN`[5] (Mann et al. 2016; Johnson et al. 2018). All the codes converge to a consistent solution for the stellar and BD parameters.

3.2. *Stellar parameters from Gaia DR2*

As an additional independent check on the derived stellar parameters, we performed an analysis of the broadband spectral energy distribution (SED) together with the *Gaia* DR2 parallax in order to determine an empirical measurement of the stellar radius, following the procedures described in Stassun & Torres (2016); Stassun et al. (2017, 2018a). We pulled the $B_T V_T$ magnitudes from *Tycho-2*, the Strömgren *ubvy* magnitudes from Paunzen (2015), the $BVgri$ magnitudes from APASS, the JHK_S magnitudes from *2MASS*, the W1–W4 magnitudes from *WISE*, and the G magnitude from *Gaia*. We also used the *GALEX* NUV and/or FUV fluxes when available. Together, the available photometry spans the full stellar SED over the wavelength range 0.35–22 μm, and extends down to 0.15 μm when *GALEX* data are available (see Figure 8). We performed a fit using Kurucz stellar atmosphere models, with the priors on effective temperature ($T_{\rm eff}$), surface gravity ($\log g$), and metallicity ([Fe/H]) from the spectroscopically determined values. The remaining free parameter is the extinction (A_V), which we restricted to the maximum line-of-sight value from the dust maps of Schlegel et al. (1998).

The resulting fit is very good (Figure 8) with a reduced χ^2 of 4.8. The best fit extinction is $A_V = 0.00^{+0.06}_{-0.00}$. Integrating the (unreddened) model SED gives the bolometric flux at Earth of $F_{\rm bol} = 4.18 \pm 0.15 \times 10^{-9}$ erg s cm^{-2}. Taking the $F_{\rm bol}$ and $T_{\rm eff}$ together with the *Gaia* DR2 parallax, adjusted by +0.08 mas to account for the systematic offset reported by Stassun & Torres (2018), gives the stellar radius as $R = 1.66 \pm 0.05$ R$_\odot$. We note that when we do not account for this systematic offset (as with our values in Table 3 and 9), we measure roughly 2.3% larger radii for the star and BD. This difference does not affect our final conclusions about this system. Finally, estimating the stellar mass from the empirical relations of Torres et al. (2010) gives $M = 1.90 \pm 0.11 M_\odot$, which with the radius gives the density $\rho = 0.58 \pm 0.06$ g cm^{-3}. We find that this independent check on the stellar mass and radius agrees with the values shown in Table 3.

[5] https://github.com/captain-exoplanet/misttborn

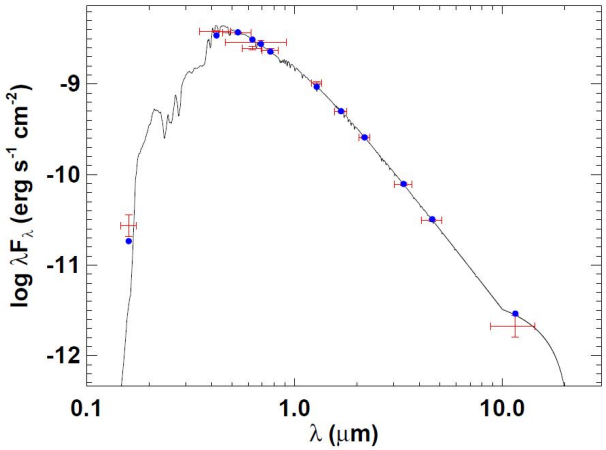

Figure 8. SED fit using *Gaia* DR2 parallax with magnitudes from *Tycho-2* ($B_T V_T$), Paunzen (2015) (Strömgren *ubvy*), APASS ($BVgri$), *2MASS* (JHK_S), *WISE* (W1–W4), and the G magnitude from *Gaia* . The SED measurements are in red with the model in blue.

3.3. *Estimating the age of the TOI-503 system*

We report an age of 180^{+170}_{-110} Myr for TOI-503 using the MIST models and `EXOFASTv2`. We find this consistent with the Yonsei Yale (YY) isochrone models (Spada et al. 2013), from which we report an age of 200^{+200}_{-130} Myr. Both the MIST and YY isochrone grids are incorporated into the framework of `EXOFASTv2`. A stellar mass track is interpolated from the grids for the MIST or YY isochrones, and from this, an age is estimated (Eastman et al. 2019). We reiterate that the metallicity range of MIST isochrones is -5.0 $\leq$ [Fe/H] $\leq$ 0.5, which may influence the accuracy of the age estimate given that we measure a spectroscopic [Fe/H] of 0.6 with `iSpec`. The YY isochrones have a metallicity range of -3.29 $\leq$ [Fe/H] $\leq$ 0.78, which makes this set of isochrones better suited to this system. Still, we find the stellar and BD properties to be consistent between the two isochrone models.

Independently from the MIST and YY models, we have the COND03 and Saumon & Marley (2008) substellar evolutionary models with which we qualitatively estimate the age of TOI-503b (Figure 9). The COND03 models present evolutionary tracks for irradiated giant

planets and BDs, making them useful in the study of short-period BDs. The Saumon & Marley (2008) models include details like metal-rich, metal-poor, and cloudy atmosphere models for low-mass stars and BDs. Given the large uncertainties in the radius of TOI-503b, we can only conclude that the BD is likely not much older than 200-300 Myr based on these substellar evolutionary models. This is consistent with the ages estimated from the MIST and YY models of the host star. The age of TOI-503b also implies that the BD is still cooling and contracting in radius. The BD cooling models from Baraffe et al. (2003) indicate that an object with a mass on the order of 10 M_J and an age greater than 500 Myr may maintain a radius of at least 1.0-1.2 R_J while in close proximity (semi-major axis of $a = 0.046$AU) to a host star with $T_{\rm eff} = 6000$K. The difference between a non-irradiated and irradiated BD at ages up to 10 Gyr is roughly 0.1 R_J (Baraffe et al. 2003). However, this is not the most appropriate comparison to TOI-503b given the large difference in the mass of the BD and $T_{\rm eff}$ of the host star. We expect a much hotter star at $T_{\rm eff} = 7650$K to have a stronger irradiative effect on the BD and lead to an inflated atmosphere, but the change in surface gravity going from a 10 M_J object to a 53 M_J object counteracts this. Given the grazing nature of the transit, however, we are limited in how thoroughly we may interpret what effects this Am star has on the radius of its substellar companion. This makes it difficult to disentangle the gradual cooling this BD has undergone from the irradiative effects of the nearby star. It is certainly possible that TOI-503 has inflated its BD, but it is not likely to be much more than the uncertainties in the radius of the BD that we measure (0.17-0.30 R_J).

However, we are confident that this is one of the youngest intermediate-mass BDs ever found. Its nearest counterparts in terms of mass are AD 3116b, which has a measured age of 600 Myr and mass of 54 M_J (Gillen et al. 2017) and EPIC 212036875b, which has a mass of 52 M_J and no directly measured age (i.e. from association with a stellar cluster). EPIC 212036875b does have an age estimated with `PARAM 1.3` of 5.1 ± 0.9 Gyr from Persson et al. (2019). The only other known BD around an A-type star is HATS-70b (Zhou et al. 2019) and this very low-mass (12.9 M_J) BD actually appears to be inflated.

4. DISCUSSION

4.1. *The transiting BD population*

The mass-period diagram of transiting BDs (Figure 10) shows a sparse but diverse population. The total number of published transiting BDs, including TOI-503b in this work, is 21 (see Table 4 for this list). The

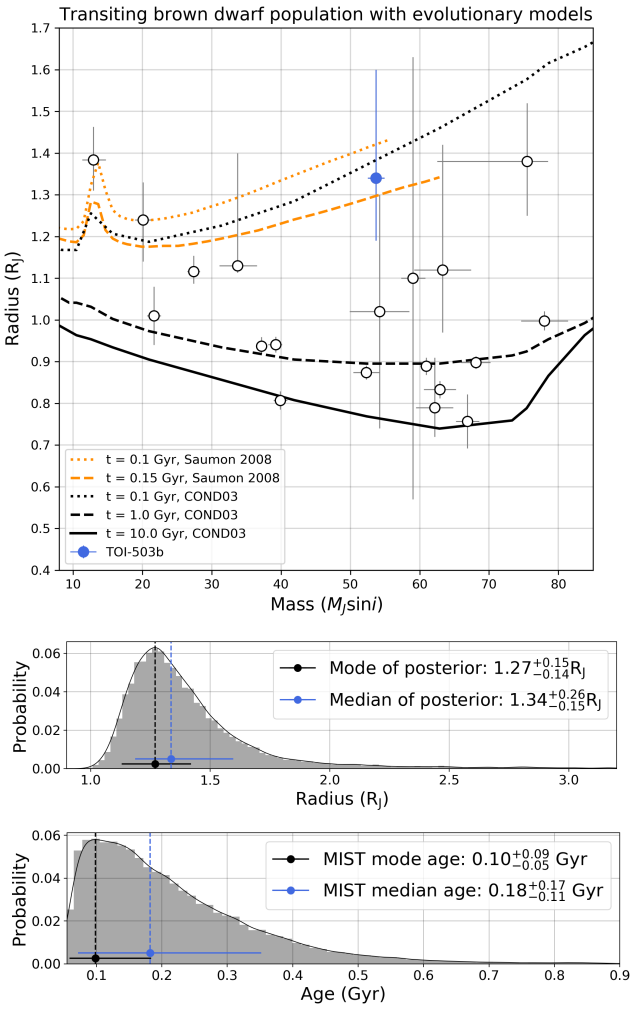

Figure 9. Top: Evolutionary brown dwarf models of mass versus radius (Baraffe et al. 2003; Saumon & Marley 2008) with known transiting BDs over plotted. We use the *median* results from `EXOFASTv2` for the mass and radius for TOI-503b in this figure. Middle: Posterior distribution of the BD radius from the `EXOFASTv2`/MIST results for TOI-503. The median value is reported in Table 6 as $1.34^{+0.26}_{-0.15}$ R_J and here, we report a value for the *mode* of the posterior distribution to be $1.30^{+0.15}_{-0.14}$ R_J. This is consistent with the posterior distribution for the BD radius using `EXOFASTv2`/YY. Bottom: The posterior distribution for the age of TOI-503 showing the mode and median values for the age of the system.

BD binary system, 2M0535-05 (Stassun et al. 2006), and the very young (~5-10 Myr) RIK 72b, which transits a pre-main sequence star (David et al. 2019), are not shown in Figure 9 because their radii are above 3 R_J and do not correspond to the Baraffe et al. (2003) and Saumon & Marley (2008) models, which consider the presence of a main sequence host star. KOI-189b (Díaz et al. 2014) has a mass of 78.0 ± 3.4 M_J and is the most massive BD while HATS-70b, with a mass of

$12.9 \pm 1.8\,M_J$, is the least massive. This neatly places objects at the two extremes in mass of what is considered a BD, but Díaz et al. (2014) caution that KOI-189b may instead be a low-mass star.

TOI-503b has an intermediate-mass of $53.7 \pm 1.2\,M_J$, an inclination angle of $82.25^{+0.31}_{-0.41}$ degrees ($b = 0.974^{+0.022}_{-0.015}$), and lies in the driest part of the brown dwarf desert (35-55 $M_J \sin i$, $P \leq 100$ days, Ma & Ge (2014b)). There is a paucity of objects detected in this driest region of the brown dwarf desert, but in recent years, 5 BDs (Gillen et al. (2017), Nowak et al. (2017), Hodžić et al. (2018), Carmichael et al. (2019), Persson et al. (2019), and this work) have been discovered in this intermediate mass-range, bringing new life, so to speak, to the desert and increasing the overall tally in the aforementioned range to 6. The recent growth in the discoveries of this type of BDs could be a hint at an undisclosed population in the driest part of the BD desert. Furthermore, based on a literature survey, we see that the projected masses of these 6 BDs are in the range of either 35-40 $M_J \sin i$ or 50-55 $M_J \sin i$. None of them belong to the mass-range of 40-50 $M_J \sin i$, which makes this the most depleted region in the transiting BDs (see Figure 10). This also indicates that the driest region of the BD desert is contracting from 35-55 $M_J \sin i$ to the 40-50 $M_J \sin i$ mass range. With the rise in the population of BDs in the intermediate mass-range, the driest region of the BD desert may further contract and eventually disappear. However, due to the current scarcity of known transiting BDs, it is difficult to confidently draw any statistically-motivated conclusions on the behavior of this population, let alone how BDs at different masses form.

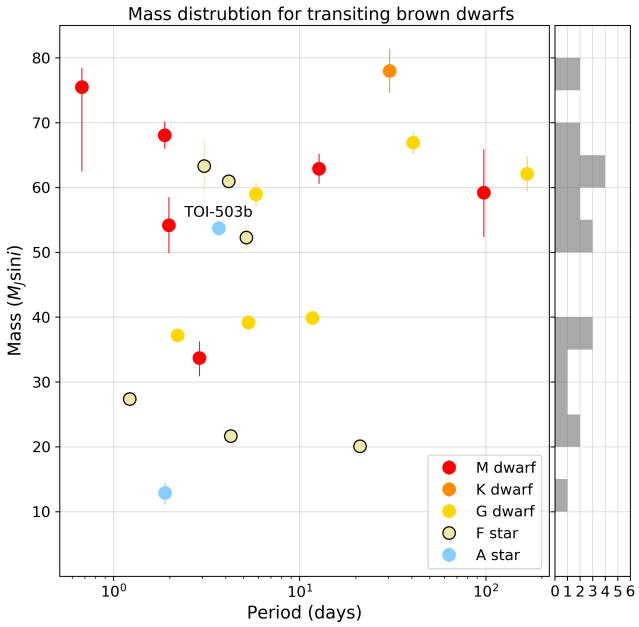

Figure 10. The mass distribution over period for transiting BDs from Table 4. The color of each point indicates the spectral type of the star that hosts the BD. The histogram of the BD mass distribution is shown in the right panel with bin sizes of $5\,M_J$. The absence of BDs in the 40-50 M_J mass range can be seen here, but we caution that this may be a result of the small number of transiting BDs (21) that have been discovered to date.

4.2. *Circularization timescales and orbital synchronization for TOI-503*

Based on our estimate of the age of TOI-503 (roughly 180 Myr) and the circular orbit of TOI-503b, we now consider the role tidal interactions have played in the orbital evolution of this system, namely, whether or not tides could have circularized the orbit of the BD. This comparison of circularization timescale to the system's age has implications for how the BD may have formed.

In order for a binary system affected by tides to be in a stable equilibrium, it must satisfy two conditions: the orbital angular momentum must be at least three times the sum of the rotational angular momenta of the two components, and the total angular momentum of the system must be greater than the critical value:

$$L_{\rm crit} = 4\left[\frac{G^2}{27}\frac{M_\star^3 M_{\rm BD}^3}{M_\star + M_{\rm BD}}(I_\star + I_{\rm BD})\right]^{\frac{1}{4}} \quad (1)$$

where $I_\star$ and $I_{\rm BD}$ are the rotational moments of inertia of the star and BD, respectively (Hut 1980). We assume a value of $I_\star = \alpha_\star M_\star R_\star^2$ where $\alpha_\star = 0.24$, interpolating the stellar moments of inertia from Claret & Gimenez (1989) to the mass of TOI-503. We assume that the BD is a uniform sphere, such that $I_{\rm BD} = 2/5 M_{\rm BD} R_{\rm BD}^2$; this is not likely to be true in detail, but $I_\star >> I_{\rm BD}$ so this assumption has a negligible effect upon our results. We additionally assume that the orbit of the BD is well-aligned to the stellar rotation, i.e. $\sin i_\star \approx 1$, in order to calculate the stellar rotation period from $v \sin i_\star$, and we assume the present-day stellar rotation rate for the quoted calculations. We find that $L_{\rm tot} = 1.07 \pm 0.07 L_{\rm crit}$, and $L_{\rm orb} = 5.0 \pm 0.5 L_{\rm rot}$. TOI-503 is thus Darwin stable; interestingly, the total angular momentum is consistent with being equal to the critical value, while the orbital angular momentum is close to twice the critical value relative to the rotational angular momentum, both much like KELT-1b (Siverd et al. 2012).

From Jackson et al. (2008), the timescale for orbital circularization timescale for a close-in companion is

$$\frac{1}{\tau_e} = \left[\frac{63}{4}\sqrt{GM_\star^3}\frac{R_{\rm BD}{}^5}{Q_{\rm BD} M_{\rm BD}} + \frac{171}{16}\sqrt{G/M_\star}\frac{R_\star^5 M_{\rm BD}}{Q_\star}\right] a^{-\frac{13}{2}} \quad (2)$$

where $Q_\star$ and $Q_{\rm BD}$ are the tidal quality factors of the star and brown dwarf, respectively. Jackson et al. (2008) did not provide an expression for the tidal synchronization timescale, but Goldreich & Soter (1966), from whom Jackson et al. (2008) obtained their expressions, did. Rewriting this expression to use the terminology of this work, the synchronization timescale is

$$\frac{1}{\tau_\Omega} = \frac{9}{4}\frac{GR_\star^3 M_{\rm BD}^2}{\alpha_\star M_\star Q_\star \Omega a^6} \quad (3)$$

where Ω is the angular velocity of the star.

In order to estimate the tidal timescales we follow (Persson et al. 2019) and adopt $Q_\star = 10^8$ and $Q_{\rm BD} = 10^5$. Although EPIC 212036875 (Persson et al. 2019) is less massive than TOI-503, Collier Cameron & Jardine (2018) did not find any significant $T_{\rm eff}$ dependence of $Q_\star$, justifying this assumption. We thus find tidal circularization and synchronization timescales are 1.4 ± 1.2 Gyr and 9.9 ± 1.2 Gyr, respectively. Although these are longer than our measured system age, implying in particular that the presence of TOI-503b could not have synchronized the rotation of its hosts star, we cannot rule out that Q might be smaller than we have assumed in these estimates and so the tidal damping more efficient. Nonetheless, this disfavors (but does not rule out) any high eccentricity migration scenario for TOI-503b.

4.3. *TOI-503 in Context among Am Star Binaries*

Am stars are commonly found in binary systems (e.g., Carquillat & Prieur 2007), and rotate more slowly than is typical for field A stars (e.g., Abt & Morrell 1995). The Am nature of these stars is thought to be due to their slow rotation and it has been hypothesized that there may be a link between the binarity and slow rotation, but the exact mechanisms involved are still not well known (e.g., Böhm-Vitense 2006). It has also been noted that not all slowly-rotating A stars are Am stars Abt (2009). While many short-period Am binary systems could have experienced tidal synchronization, a significant number of Am binaries are too widely separated to experience significant tidal effects within their main sequence lifetimes (Carquillat & Prieur 2007). Due to the small mass ratio of TOI-503, the latter class is more likely, i.e. the slow rotation of the Am star cannot be attributed to tidal effects. Instead, the slow rotation is likely to be due to some facet of the star formation process; perhaps in these binaries most of the angular momentum of the protostellar disk was taken up by the mutual orbit of the binary components, rather than going into their rotation. In the case of TOI-503, if all of the angular momentum of the system were to be deposited into the primary star's rotation, it would have an equatorial velocity of ~ 171 km s^{-1}, much more typical for an A star (e.g., Zorec & Royer 2012). The TOI-503 system does not stand out significantly from the known population of Am binaries.

In Figure 11, we show the mass ratios $q = M_2/M_1$ for the population of Am star binaries as a function of the orbital period. Most of the known systems are single-lined spectroscopic binaries (SB1s) for which we can only obtain a limit on the mass ratio, but we can nonetheless calculate

$$q \sin i = \frac{K_1^2 (1-e^2) a \sin i}{4\pi^2 M_1} \quad (4)$$

where we work in units of AU, $M_\odot$, and yr. There are many known Am binaries over a wide range of periods which have $q \sin i$ values as low as or lower than TOI-503. However, this is at least partly linked with small *sini* values for close to face-on systems. The mass ratio distribution obtained in the Boffin (2010) seems to slightly hint at a double-peaked distribution, with a broad peaks around q∼0.3 (for SB1s) and q∼1 (for double-lined spectroscopic binaries - SB2s).

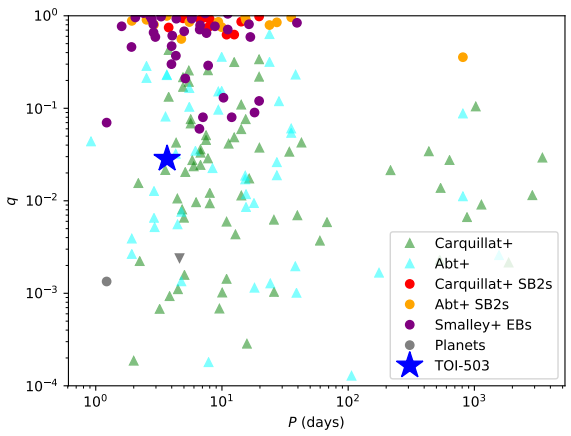

Figure 11. TOI-503 in context among the population of Am star binaries from Abt & Levy (1985), Carquillat & Prieur (2007), and Smalley et al. (2014), as well as the planets WASP-33b and KELT-19Ab. The circles show SB2s where we can obtain the mass ratio directly from the ratio of radial velocity semi-amplitudes, while the triangles show SB1s where we can only obtain $q \sin i$, which is the quantity plotted in these cases; these should therefore be regarded as lower limits. TOI-503's mass ratio is small, but many other Am star binaries have $q \sin i$ values as low or lower.

Apart from TOI-503, other Am stars known to host a low mass companion ($M_b < 80\,M_{\rm J}$), are WASP-33 (Collier Cameron et al. 2010b) and KELT-19A (Siverd et al. 2018), but the mass ratio q for both the systems is even smaller than the TOI-503 system.

4.4. *Did TOI-503b form in-situ?*

The age of TOI-503 is approximately 180 Myr. In section 4.2, we have shown that the circularization timescale for TOI-503 is longer than the likely age of the system and yet, we measure the orbit of the BD to be circular. Our interpretation of this is that TOI-503b more likely formed *in-situ* rather than ex-situ. Not enough time has passed for the BD to have formed much farther from its host star via core accretion from a protoplanetary disk and subsequently migrate inwards (unless that migration was very quick) where the tidal forces of the star would eventually circularize the BD's orbit. Instead, TOI-503b may have followed a formation path more similar to that of a low-mass star and it may have formed in an orbital configuration very similar to the one we observe here. This may imply a favored formation mechanism for other BDs at this mass regime that orbit stars in short periods. However, as we have mentioned, with so few transiting BDs available for the type of detailed study presented here, we cannot conclude that intermediate-mass BDs form more favorably through a mechanism similar to that of low-mass stars.

To address this point, we can look at the two nearest neighbors, in terms of mass, to TOI-503b: AD 3116b and EPIC 212036875b. As shown in two independent studies (Carmichael et al. 2019; Persson et al. 2019), EPIC 212036875b is an eccentric ($e = 0.132$), short-period ($P = 5.16$ days) BD that orbits an F-type star. The Persson et al. (2019) study found EPIC 212036875b to likely have formed ex-situ via gravitational disk instabilities and then quickly migrate to its current, close-in eccentric orbit. For AD 3116b, the circularization timescale is challenging to interpret, as Gillen et al. (2017) caution, given the mass ratio of this system ($q \approx 0.18$), the very short (< 2 days) period, and the nature of the host M dwarf star. Though AD 3116b is young at a measured age of 600 Myr, given the nature of its orbit and host star, it is more difficult to infer a formation scenario in the same way we do for TOI-503b. This highlights how the mass of a short-period BD may not as strongly dictate a formation scenario (in-situ versus ex-situ) as any single discovery might imply. Ultimately, we find TOI-503b to be a particularly special kind of BD in the context of the known transiting BD population and it serves as one of the first examples of a BD for which we have evidence for an in-situ formation scenario.

The in-situ formation scenario also points to a possible way that Am stars can form. To our knowledge, this is the first time a BD has been detected orbiting an Am star in such a short-period. Detailed studies of Am stars report a binary fraction around 60-70% (Abt & Levy 1985; Carquillat & Prieur 2007). In some such systems, the stellar companions are too distant for the tidal braking to be effective (e.g., Siverd et al. 2018). It possibly suggests that other processes may need to be invoked to explain their small rotational velocities. However, this may also be linked to the fact that it is difficult to detect such a low mass star as a BD around an Am star and our discovery of one such BD around an Am star in the BD desert goes in this direction. Further similar discoveries are however needed to confirm if this is the correct solution. The BD orbiting an Am star is a bridge connecting two areas that are not fully understood: the formation mechanisms and ultimate classification of BDs, and the creation, evolution, and behavior of Am stars. Such an overlap enables us to look at these areas from an entirely new perspective.

5. SUMMARY

We have presented the analysis of the first BD known to transit an Am star, TOI-503b. This is the newest member of the brown dwarf desert and it orbits its host star in a circular, short-period ($P = 3.67718 \pm 0.0001$ days) orbit. We measure the host star to have a mass of $M_\star = 1.80 \pm 0.06\,M_\odot$, a radius of $R_\star = 1.70 \pm 0.05\,R_\odot$, an effective temperature of $T_{\rm eff} = 7650 \pm 160$K, and metallicity of 0.6 ± 0.1 dex. The transit geometry of the system is grazing as revealed by the TESS light curve and confirmed by the DT analysis of the high-resolution spectra, acquired during primary transit, from Tautenberg observatory. The BD has a radius of $R_b = 1.34^{+0.26}_{-0.15}\,\mathrm{R_J}$ and mass of $M_b = 53.7 \pm 1.2\,\mathrm{M_J}$, which places it in the driest part of the BD desert. We find that with the recent growth in the population of this kind of BDs, the driest region of the desert is contracting from $35 - 55 M_J \sin i$ to $40 - 50 M_J \sin i$. The age of the system is estimated to be ∼180 Myr using MIST and YY isochrones and is much younger than the theoretical tidal circularization and synchronization timescales of the system. This favors an in-situ formation scenario for the BD but does not strongly rule out an ex-situ formation scenario as with EPIC 212036875b. Due to the smaller mass ratio of the system, we attribute the slow rotation of the host star to be caused by some other primordial feature of the system and not from tidal interactions from the BD.

6. ACKNOWLEDGEMENTS

J.Š. and P.K. would like to acknowledge the support from GACR international grant 17-01752J. J.Š. would like to acknowledge the support from source 116-09/260441, Institute of Theoretical Physics, Charles

University in Prague, Czech Republic. J.K., S.G., M.P., S.C., A.P.H., H.R., M.E. and K.W.F.L. acknowledge support by Deutsche Forschungsgemeinschaft (DFG) grants PA525/18-1, PA525/19-1, PA525/20-1, HA 3279/12-1, and RA 714/14-1 within the DFG Schwerpunkt SPP 1992, Exploring the Diversity of Extrasolar Planets. S.C. acknowledges the Hungarian Scientific Research Fund (OTKA) Grant KH-130372. This work is partly supported by JSPS KAKENHI Grant Numbers JP18H01265 and JP18H05439, and JST PRESTO Grant Number JPMJPR1775. S.M. acknowledges support by the Spanish Ministry through the Ramon y Cajal fellowship number RYC-2015-17697. R.A.G. acknowledges the support from the PLATO/CNES grant. M.S. acknowledges the Postdoc@MUNI project CZ.02.2.69/0.0/0.0/16-027/0008360. M.F., C.M.P. and I.G. gratefully acknowledge the support of the Swedish National Space Agency (DNR 163/16 and 174/18). K.G.S. acknowledges partial support from NASA grant 17-XRP17 2-0024. This paper includes data collected by the *Kepler* mission. Funding for the *Kepler* mission is provided by the NASA Science Mission directorate. Some of the data presented in this paper were obtained from the Mikulski Archive for Space Telescopes (MAST). STScI is operated by the Association of Universities for Research in Astronomy, Inc., under NASA contract NAS5-26555. Based on observations made with the Nordic Optical Telescope, operated by the Nordic Optical Telescope Scientific Association at the Observatorio del Roque de los Muchachos, La Palma, Spain, of the Instituto de Astrofísica de Canarias. T.C. would like to acknowledge the effort of the observers who acquired the ground-based photometry at FLWO, LCO, CHAT, and FLI as part of the TESS Follow-up Program. Thanks to Scott Gaudi for useful discussions. The PARAS spectrograph is fully funded and being supported by Physical Research Laboratory (PRL), which is part of Department of Space, Government of India. R.S. and A.C. would like to thank Director, PRL for his support and acknowledges the help from Vishal Shah and Mount Abu Observatory staff at the time of observations. A.C. is grateful to Suvrath Mahadevan from Pennsylvania University, USA and Arpita Roy from Caltech, USA for their tremendous efforts in the development of the PARAS data pipeline.

REFERENCES

Abt, H. A. 2009, AJ, 138, 28

Abt, H. A., & Levy, S. G. 1985, ApJS, 59, 229

Abt, H. A., & Morrell, N. I. 1995, ApJS, 99, 135

Abt, H. A., & Moyd, K. I. 1973, ApJ, 182, 809

Aigrain, S., Llama, J., Ceillier, T., et al. 2015, MNRAS, 450, 3211

Albrecht, S., Reffert, S., Snellen, I., Quirrenbach, A., & Mitchell, D. S. 2007, A&A, 474, 565

Alsubai, K., Tsvetanov, Z. I., Latham, D. W., et al. 2018, AJ, 155, 52

Anderson, D. R., Collier Cameron, A., Hellier, C., et al. 2011, ApJL, 726, L19

Balona, L. A. 2011, MNRAS, 415, 1691

—. 2013, MNRAS, 431, 2240

—. 2017, MNRAS, 467, 1830

Balona, L. A., Catanzaro, G., Abedigamba, O. P., Ripepi, V., & Smalley, B. 2015, MNRAS, 448, 1378

Baraffe, I., Chabrier, G., Allard, F., & Hauschildt, P. H. 2002, A&A, 382, 563

Baraffe, I., Chabrier, G., Barman, T. S., Allard, F., & Hauschildt, P. H. 2003, A&A, 402, 701

Barragán, O., Gandolfi, D., & Antoniciello, G. 2019, MNRAS, 482, 1017

Bayliss, D., Hojjatpanah, S., Santerne, A., et al. 2017, AJ, 153, 15

Blanco-Cuaresma, S. 2019, MNRAS, 486, 2075

Blanco-Cuaresma, S., Soubiran, C., Heiter, U., & Jofré, P. 2014, A&A, 569, A111

Boffin, H. M. J. 2010, A&A, 524, A14

Böhm, T., Holschneider, M., Lignières, F., et al. 2015, A&A, 577, A64

Böhm-Vitense, E. 2006, PASP, 118, 419

Bonomo, A. S., Sozzetti, A., Santerne, A., et al. 2015, A&A, 575, A85

Borucki, W. J., Koch, D., Basri, G., et al. 2010, Science, 327, 977

Bouchy, F., Deleuil, M., Guillot, T., et al. 2011a, A&A, 525, A68

Bouchy, F., Bonomo, A. S., Santerne, A., et al. 2011b, A&A, 533, A83

Bressan, A., Marigo, P., Girardi, L., et al. 2012, MNRAS, 427, 127

Buchhave, L. A., Bakos, G. Á., Hartman, J. D., et al. 2010, ApJ, 720, 1118

Buchhave, L. A., Latham, D. W., Johansen, A., et al. 2012, Nature, 486, 375

Carmichael, T., Latham, D., & Vanderburg, A. 2019, arXiv e-prints, arXiv:1903.03118

Carquillat, J.-M., & Prieur, J.-L. 2007, MNRAS, 380, 1064

Cayrel, R., van't Veer-Menneret, C., Allard, N. F., & Stehlé, C. 2011, A&A, 531, A83
Ceillier, T., van Saders, J., García, R. A., et al. 2016, MNRAS, 456, 119
Ceillier, T., Tayar, J., Mathur, S., et al. 2017, A&A, 605, A111
Chakraborty, A., Mahadevan, S., Roy, A., et al. 2014, PASP, 126, 133
Chaturvedi, P., Chakraborty, A., Anand arao, B. G., Roy, A., & Mahadevan, S. 2016, MNRAS, 462, 554
Chaturvedi, P., Sharma, R., Chakraborty, A., Anandarao, B. G., & Prasad, N. J. S. S. V. 2018, AJ, 156, 27
Choi, J., Dotter, A., Conroy, C., et al. 2016, ApJ, 823, 102
Claret, A. 2017, A&A, 600, A30
Claret, A., & Gimenez, A. 1989, A&AS, 81, 37
Collier Cameron, A., Bruce, V. A., Miller, G. R. M., Triaud, A. H. M. J., & Queloz, D. 2010a, MNRAS, 403, 151
Collier Cameron, A., Horne, K., Penny, A., & Leigh, C. 2002, MNRAS, 330, 187
Collier Cameron, A., & Jardine, M. 2018, MNRAS, 476, 2542
Collier Cameron, A., Guenther, E., Smalley, B., et al. 2010b, MNRAS, 407, 507
Csizmadia, S., & CoRot Team. 2016, III.6 Exploration of the brown dwarf regime around solar-like stars by CoRoT, 143
Csizmadia, S., Hatzes, A., Gandolfi, D., et al. 2015a, A&A, 584, A13
—. 2015b, A&A, 584, A13
Cutri, R. M., & et al. 2013, VizieR Online Data Catalog, 2328
Cutri, R. M., Skrutskie, M. F., van Dyk, S., et al. 2003, VizieR Online Data Catalog, 2246
da Silva, L., Girardi, L., Pasquini, L., et al. 2006, A&A, 458, 609
David, T. J., Hillenbrand, L. A., Gillen, E., et al. 2019, ApJ, 872, 161
Deleuil, M., Deeg, H. J., Alonso, R., et al. 2008, A&A, 491, 889
Díaz, R. F., Damiani, C., Deleuil, M., et al. 2013, A&A, 551, L9
Díaz, R. F., Montagnier, G., Leconte, J., et al. 2014, A&A, 572, A109
Dotter, A. 2016, ApJS, 222, 8
Eastman, J. D., Rodriguez, J. E., Agol, E., et al. 2019, arXiv e-prints, arXiv:1907.09480
Frandsen, S., & Lindberg, B. 1999, in Astrophysics with the NOT, ed. H. Karttunen & V. Piirola, 71
Furlan, E., Ciardi, D. R., Everett, M. E., et al. 2017, VizieR Online Data Catalog, J/AJ/153/71
Gandolfi, D., Parviainen, H., Deeg, H. J., et al. 2015, A&A, 576, A11
Gandolfi, D., Fossati, L., Livingston, J. H., et al. 2019, ApJL, 876, L24
García, R. A., Mathur, S., Pires, S., et al. 2014a, A&A, 568, A10
García, R. A., Ceillier, T., Salabert, D., et al. 2014b, A&A, 572, A34
Gibson, N. P., Aigrain, S., Roberts, S., et al. 2012, MNRAS, 419, 2683
Gillen, E., Hillenbrand, L. A., David, T. J., et al. 2017, ApJ, 849, 11
Goldreich, P., & Soter, S. 1966, Icarus, 5, 375
Grether, D., & Lineweaver, C. H. 2006, ApJ, 640, 1051
Gustafsson, B., Edvardsson, B., Eriksson, K., et al. 2008, A&A, 486, 951
Hatzes, A. P. 1998, A&A, 330, 541
Hatzes, A. P., & Rauer, H. 2015, ApJL, 810, L25
Heiter, U., Lind, K., Asplund, M., et al. 2015, PhyS, 90, 054010
Hjorth, M., Justesen, A. B., Hirano, T., et al. 2019, MNRAS, 484, 3522
Hodžić, V., Triaud, A. H. M. J., Anderson, D. R., et al. 2018, MNRAS, 481, 5091
Høg, E., Fabricius, C., Makarov, V. V., et al. 2000, A&A, 357, 367
Hut, P. 1980, A&A, 92, 167
Irwin, J., Buchhave, L., Berta, Z. K., et al. 2010, ApJ, 718, 1353
Irwin, J. M., Charbonneau, D., Esquerdo, G. A., et al. 2018, AJ, 156, 140
Jackman, J. A. G., Wheatley, P. J., Bayliss, D., et al. 2019, arXiv e-prints, arXiv:1906.08219
Jackson, B., Greenberg, R., & Barnes, R. 2008, ApJ, 678, 1396
Jenkins, J. M., Twicken, J. D., McCauliff, S., et al. 2016, in Proc. SPIE, Vol. 9913, Software and Cyberinfrastructure for Astronomy IV, 99133E
Johnson, J. A., Apps, K., Gazak, J. Z., et al. 2011, ApJ, 730, 79
Johnson, M. C., Dai, F., Justesen, A. B., et al. 2018, MNRAS, 481, 596
Kabáth, P., Skarka, M., Sabotta, S., & Guenther, E. 2019a, Contributions of the Astronomical Observatory Skalnate Pleso, 49, 462
Kabáth, P., Žák, J., Boffin, H. M. J., et al. 2019b, PASP, 131, 085001
Korth, J., Csizmadia, S., Gandolfi, D., et al. 2019, MNRAS, 482, 1807

Kurucz, R. L. 1993, SYNTHE spectrum synthesis programs and line data
Lindegren, L., Hernández, J., Bombrun, A., et al. 2018, A&A, 616, A2
Livingston, J. H., Dai, F., Hirano, T., et al. 2019, MNRAS, 484, 8
Lucy, L. B., & Sweeney, M. A. 1971, AJ, 76, 544
Ma, B., & Ge, J. 2014a, MNRAS, 439, 2781
—. 2014b, MNRAS, 439, 2781
Mann, A. W., Gaidos, E., Mace, G. N., et al. 2016, ApJ, 818, 46
Mathur, S., García, R. A., Régulo, C., et al. 2010, A&A, 511, A46
Mathur, S., García, R. A., Ballot, J., et al. 2014, A&A, 562, A124
McQuillan, A., Mazeh, T., & Aigrain, S. 2014, ApJS, 211, 24
Meschiari, S., Wolf, A. S., Rivera, E., et al. 2009, PASP, 121, 1016
Michaud, G., Tarasick, D., Charland, Y., & Pelletier, C. 1983, ApJ, 269, 239
Moutou, C., Bonomo, A. S., Bruno, G., et al. 2013, A&A, 558, L6
Nowak, G., Palle, E., Gandolfi, D., et al. 2017, AJ, 153, 131
Palle, E., Nowak, G., Luque, R., et al. 2019, A&A, 623, A41
Paunzen, E. 2015, A&A, 580, A23
Paxton, B., Marchant, P., Schwab, J., et al. 2015, ApJS, 220, 15
Persson, C. M., Csizmadia, S., Mustill, A. J., et al. 2019, A&A, 628, A64
Petit, P., Hébrard, E. M., Böhm, T., Folsom, C. P., & Lignières, F. 2017, MNRAS, 472, L30
Piskunov, N. E., & Valenti, J. A. 2002, A&A, 385, 1095
Ricker, G. R., Winn, J. N., Vanderspek, R., et al. 2015, Journal of Astronomical Telescopes, Instruments, and Systems, 1, 014003
Rouan, D., Baglin, A., Copet, E., et al. 1998, Earth Moon and Planets, 81, 79
Sabotta, S., Kabath, P., Korth, J., et al. 2019, MNRAS, arXiv:1908.04570
Sahlmann, J., Ségransan, D., Queloz, D., et al. 2011, A&A, 525, A95
Santos, A. R. G., García, R. A., Mathur, S., et al. 2019, arXiv e-prints, arXiv:1908.05222
Saumon, D., & Marley, M. S. 2008, ApJ, 689, 1327
Schlegel, D. J., Finkbeiner, D. P., & Davis, M. 1998, ApJ, 500, 525
Siverd, R. J., Beatty, T. G., Pepper, J., et al. 2012, ApJ, 761, 123
Siverd, R. J., Collins, K. A., Zhou, G., et al. 2018, AJ, 155, 35
Skarka, M., Kabáth, P., Paunzen, E., et al. 2019, MNRAS, 487, 4230
Skrzypek, N., Warren, S. J., & Faherty, J. K. 2016, A&A, 589, A49
Smalley, B., Southworth, J., Pintado, O. I., et al. 2014, A&A, 564, A69
Spada, F., Demarque, P., Kim, Y.-C., & Sills, A. 2013, ApJ, 776, 87
Spiegel, D. S., Burrows, A., & Milsom, J. A. 2011, ApJ, 727, 57
Stassun, K. G., Collins, K. A., & Gaudi, B. S. 2017, AJ, 153, 136
Stassun, K. G., Corsaro, E., Pepper, J. A., & Gaudi, B. S. 2018a, AJ, 155, 22
Stassun, K. G., Mathieu, R. D., & Valenti, J. A. 2006, Nature, 440, 311
Stassun, K. G., & Torres, G. 2016, arXiv e-prints, arXiv:1609.05390
—. 2018, ApJ, 862, 61
Stassun, K. G., Oelkers, R. J., Pepper, J., et al. 2018b, AJ, 156, 102
—. 2019, VizieR Online Data Catalog, J/AJ/156/102
Telting, J. H., Avila, G., Buchhave, L., et al. 2014, Astronomische Nachrichten, 335, 41
Tody, D. 1993, in Astronomical Society of the Pacific Conference Series, Vol. 52, Astronomical Data Analysis Software and Systems II, ed. R. J. Hanisch, R. J. V. Brissenden, & J. Barnes, 173
Torrence, C., & Compo, G. P. 1998, Bulletin of the American Meteorological Society, 79, 61
Torres, G., Andersen, J., & Giménez, A. 2010, A&A Rv, 18, 67
Udry, S., Mayor, M., & Queloz, D. 1999, in Astronomical Society of the Pacific Conference Series, Vol. 185, IAU Colloq. 170: Precise Stellar Radial Velocities, ed. J. B. Hearnshaw & C. D. Scarfe, 367
van Dokkum, P. G. 2001, PASP, 113, 1420
Whitworth, A. 2018, arXiv e-prints, arXiv:1811.06833
Wizinowich, P., Acton, D. S., Shelton, C., et al. 2000, PASP, 112, 315
Zhou, G., Bakos, G. Á., Bayliss, D., et al. 2018, arXiv e-prints, arXiv:1811.06925
Zhou, G., Bakos, G. Á., Bayliss, D., et al. 2019, The Astronomical Journal, 157, 31. https://doi.org/10.3847%2F1538-3881%2Faaf1bb
Zorec, J., & Royer, F. 2012, A&A, 537, A120

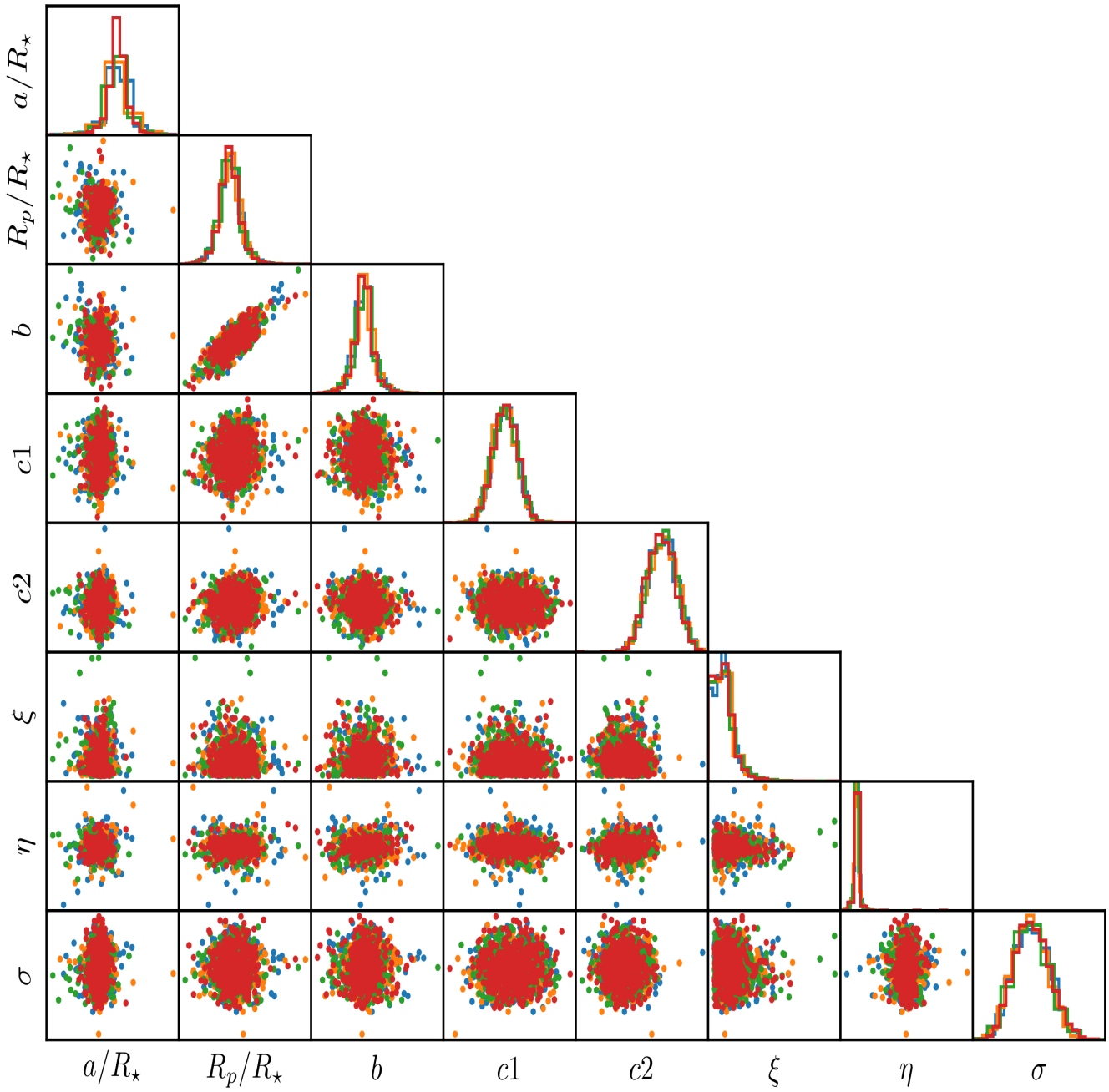

Figure 12. The correlations between the free parameters of the LC model from the MCMC analysis using the `GeePea` code. At the end of each row is shown the derived posterior probability distribution. We use the quadratic limb-darkening law with the coefficients c_1 and c_2. ξ, η, σ are the parameters of the noise model. The four different colours represent samples from the independent MCMC chains.

Table 4. List of published transiting brown dwarfs as of June 2019.

Name	P (days)	M_{BD}/M_J	R_{BD}/R_J	e	$M_\star/M_\odot$	$R_\star/R_\odot$	T_{eff}(K)	[Fe/H]	Reference
TOI-503b	3.677	53.7 ± 1.2	$1.34^{+0.26}_{-0.15}$	0 (adopted)	1.80 ± 0.06	1.70 ± 0.05	7650 ± 160	$+0.61 \pm 0.07$	this work
HATS-70b	1.888	$12.9^{+1.8}_{-1.6}$	$1.38^{+0.08}_{-0.07}$	< 0.18	1.78 ± 0.12	$1.88^{+0.06}_{-0.07}$	7930^{+630}_{-820}	$+0.04 \pm 0.11$	1
KELT-1b	1.218	27.4 ± 0.9	1.12 ± 0.04	0.01 ± 0.01	1.34 ± 0.06	1.47 ± 0.05	6516 ± 49	$+0.05 \pm 0.08$	2
NLTT 41135b	2.889	33.7 ± 2.8	1.13 ± 0.27	< 0.02	0.19 ± 0.03	0.21 ± 0.02	3230 ± 130	-0.25 ± 0.25	3
LHS 6343c	12.713	62.9 ± 2.3	0.83 ± 0.02	0.056 ± 0.032	0.37 ± 0.01	0.38 ± 0.01	-	$+0.02 \pm 0.19$	4
LP 261-75b	1.882	68.1 ± 2.1	0.90 ± 0.02	< 0.007	0.30 ± 0.02	0.31 ± 0.01	3100 ± 50	-	5
WASP-30b	4.157	61.0 ± 0.9	0.89 ± 0.02	0 (adopted)	1.17 ± 0.03	1.30 ± 0.02	6201 ± 97	-0.08 ± 0.10	6
WASP-128b	2.209	37.2 ± 0.9	0.94 ± 0.02	< 0.007	1.16 ± 0.04	1.15 ± 0.02	5950 ± 50	$+0.01 \pm 0.12$	7
CoRoT-3b	4.257	21.7 ± 1.0	1.01 ± 0.07	0 (adopted)	1.37 ± 0.09	1.56 ± 0.09	6740 ± 140	-0.02 ± 0.06	8
CoRoT-15b	3.060	63.3 ± 4.1	1.12 ± 0.30	0 (adopted)	1.32 ± 0.12	1.46 ± 0.31	6350 ± 200	$+0.10 \pm 0.20$	9
CoRoT-33b	5.819	59.0 ± 1.8	1.10 ± 0.53	0.070 ± 0.002	0.86 ± 0.04	0.94 ± 0.14	5225 ± 80	$+0.44 \pm 0.10$	10
Kepler-39b	21.087	20.1 ± 1.3	1.24 ± 0.10	0.112 ± 0.057	1.29 ± 0.07	1.40 ± 0.10	6350 ± 100	$+0.10 \pm 0.14$	11
KOI-189b	30.360	78.0 ± 3.4	1.00 ± 0.02	0.275 ± 0.004	0.76 ± 0.05	0.73 ± 0.02	4952 ± 40	-0.07 ± 0.12	12
KOI-205b	11.720	39.9 ± 1.0	0.81 ± 0.02	< 0.031	0.92 ± 0.03	0.84 ± 0.02	5237 ± 60	$+0.14 \pm 0.12$	13
KOI-415b	166.788	62.1 ± 2.7	0.79 ± 0.12	0.689 ± 0.001	0.94 ± 0.06	1.15 ± 0.15	5810 ± 80	-0.24 ± 0.11	14
EPIC 201702477b	40.737	66.9 ± 1.7	0.76 ± 0.07	0.228 ± 0.003	0.87 ± 0.03	0.90 ± 0.06	5517 ± 70	-0.16 ± 0.05	15
EPIC 212036875b	5.170	52.3 ± 1.9	0.87 ± 0.02	0.132 ± 0.004	1.29 ± 0.07	1.50 ± 0.03	6238 ± 60	$+0.01 \pm 0.10$	18, 21
AD 3116b	1.983	54.2 ± 4.3	1.02 ± 0.28	0.146 ± 0.024	0.28 ± 0.02	0.29 ± 0.08	3200 ± 200	$+0.16 \pm 0.10$	17
CWW 89Ab	5.293	39.2 ± 1.1	0.94 ± 0.02	0.189 ± 0.002	1.10 ± 0.05	1.03 ± 0.02	5755 ± 49	$+0.20 \pm 0.09$	16, 18
RIK 72b	97.760	59.2 ± 6.8	3.10 ± 0.31	0.146 ± 0.012	0.44 ± 0.04	0.96 ± 0.10	3349 ± 142	-	19
NGTS-7Ab	0.676	$75.5^{+3.0}_{-13.7}$	$1.38^{+0.13}_{-0.14}$	0 (adopted)	0.48 ± 0.13	0.61 ± 0.06	3359 ± 106	-	20
2M0535-05a	9.779	56.7 ± 4.8	6.50 ± 0.33	0.323 ± 0.006	-	-	-	-	22
2M0535-05b	9.779	35.6 ± 2.8	5.00 ± 0.25	0.323 ± 0.006	-	-	-	-	22

NOTE—References: 1 - Zhou et al. (2019), 2 - Siverd et al. (2012), 3 - Irwin et al. (2010), 4 - Johnson et al. (2011), 5 - Irwin et al. (2018), 6 - Anderson et al. (2011), 7 - Hodžić et al. (2018), 8 - Deleuil et al. (2008), 9 - Bouchy et al. (2011a), 10 - Csizmadia et al. (2015b), 11 - Bonomo et al. (2015), 12 - Díaz et al. (2014), 13 - Díaz et al. (2013), 14 - Moutou et al. (2013), 15 - Bayliss et al. (2017), 16 - Nowak et al. (2017), 17 - Gillen et al. (2017), 18 - Carmichael et al. (2019), 19 - David et al. (2019), 20 - Jackman et al. (2019), 21 - Persson et al. (2019)
, 22 - Stassun et al. (2006).

Table 5. Additional information on published transiting brown dwarfs.

Name	α_{J2000}	δ_{J2000}	V (magnitude)	Reference
TOI-503	08 17 16.89	12 36 04.76	9.40	this work
LP 261-75	09 51 04.58	+35 58 09.47	15.43	Irwin et al. (2018)
NLTT 41135	15 46 04.30	+04 41 30.06	18.00	Irwin et al. (2010)
LHS 6343	19 10 14.28	+46 57 24.11	13.39	Johnson et al. (2011)
KELT-1	00 01 26.92	+39 23 01.70	10.70	Siverd et al. (2012)
HATS-70	07 16 25.08	−31 14 39.86	12.57	Zhou et al. (2018)
WASP-30	23 53 38.03	−10 07 05.10	12.00	Anderson et al. (2011)
WASP-128	11 31 26.10	−41 41 22.30	12.50	Hodžić et al. (2018)
CoRoT-3	19 28 13.26	+00 07 18.70	13.29	Deleuil et al. (2008)
CoRoT-15	06 28 27.82	+06 11 10.47	16.00	Bouchy et al. (2011a)
CoRoT-33	18 38 33.91	+05 37 28.97	14.70	Csizmadia et al. (2015b)
Kepler-39	19 47 50.46	+46 02 03.49	14.47	Bouchy et al. (2011b)
KOI-189[c]	18 59 31.19	+49 16 01.17	14.74	Díaz et al. (2014)
KOI-205	19 41 59.20	+42 32 16.41	14.85	Díaz et al. (2013)
KOI-415	19 33 13.45	+41 36 22.93	14.34	Moutou et al. (2013)
EPIC 201702477	11 40 57.79	+03 40 53.70	14.57	Bayliss et al. (2017)
EPIC 212036875	08 58 45.67	+20 52 08.73	10.95	Persson et al. (2019)
CWW 89A	19 17 34.04	−16 52 17.80	12.54	Nowak et al. (2017)
AD 3116	08 42 39.43	+19 24 51.90	18.73	Gillen et al. (2017)
NGTS-7A	23 30 05.2	-38 58 11.71	15.50	Jackman et al. (2019)
RIK 72	16 03 39.22	−18 51 29.72	16.01	David et al. (2019)
2M0535-05[a]	05 35 21.85	−05 46 08.56	18.94G[b]	Stassun et al. (2006)

NOTE—a – The 2M0535-05 system is a brown dwarf binary, b – G-band magnitude from the *Gaia* mission

Table 6. Median values and 68% confidence interval for TOI-503, created using `EXOFASTv2` commit number 65aa674.

Parameter	Units	Values				
Stellar Parameters:						
M_*	Mass ($M_\odot$)	$1.80^{+0.06}_{-0.06}$				
R_*	Radius ($R_\odot$)	$1.70^{+0.05}_{-0.04}$				
L_*	Luminosity ($L_\odot$)	$8.96^{+0.54}_{-0.54}$				
ρ_*	Density (cgs)	$0.51^{+0.04}_{-0.05}$				
$\log g$	Surface gravity (cgs)	$4.23^{+0.03}_{-0.03}$				
$T_{\rm eff}$	Effective Temperature (K)	7650^{+140}_{-160}				
[Fe/H]	Metallicity (dex)	$0.30^{+0.08}_{-0.09}$				
Age	Age (Gyr)	$0.18^{+0.17}_{-0.11}$				
EEP	Equal Evolutionary Point	292^{+22}_{-31}				
A_V	V-band extinction (mag)	$0.038^{+0.028}_{-0.026}$				
σ_{SED}	SED photometry error scaling	$3.9^{+1.7}_{-0.99}$				
ϖ	Parallax (mas)	$3.878^{+0.059}_{-0.058}$				
d	Distance (pc)	$257.9^{+3.9}_{-3.8}$				
Brown Dwarf Parameters:		b				
P	Period (days)	3.67718 ± 0.00010				
R_b	Radius (R_J)	$1.34^{+0.26}_{-0.15}$				
T_C	Time of conjunction (BJD_{TDB})	$2458492.05383 \pm 0.00053$				
T_0	Optimal conjunction Time (BJD_{TDB})	$2458506.76256 \pm 0.00039$				
a	Semi-major axis (AU)	0.05727 ± 0.00063				
i	Inclination (Degrees)	$82.25^{+0.31}_{-0.41}$				
T_{eq}	Equilibrium temperature (K)	2011^{+27}_{-28}				
M_b	Mass (M_J)	53.7 ± 1.2				
K	RV semi-amplitude (m/s)	4640^{+30}_{-27}				
$logK$	Log of RV semi-amplitude	$3.6673^{+0.0028}_{-0.0026}$				
R_b/R_*	Radius of planet in stellar radii	$0.0805^{+0.015}_{-0.0090}$				
a/R_*	Semi-major axis in stellar radii	$7.22^{+0.20}_{-0.22}$				
δ	Transit depth (fraction)	$0.0065^{+0.0028}_{-0.0014}$				
$Depth$	Flux decrement at mid transit	$0.00452^{+0.00026}_{-0.00023}$				
τ	Ingress/egress transit duration (days)	$0.03836^{+0.00060}_{-0.00057}$				
T_{14}	Total transit duration (days)	$0.0767^{+0.0012}_{-0.0011}$				
b	Transit Impact parameter	$0.974^{+0.022}_{-0.015}$				
$\delta_{S,3.6\mu m}$	Blackbody eclipse depth at 3.6μm (ppm)	700^{+320}_{-160}				
$\delta_{S,4.5\mu m}$	Blackbody eclipse depth at 4.5μm (ppm)	860^{+390}_{-200}				
ρ_b	Density (cgs)	27^{+13}_{-11}				
$logg_P$	Surface gravity	$4.87^{+0.12}_{-0.17}$				
$M_P \sin i$	Minimum mass (M_J)	53.2 ± 1.2				
M_P/M_*	Mass ratio	$0.02844^{+0.00039}_{-0.00037}$				
c_1	linear limb-darkening coeff	$0.146^{+0.049}_{-0.050}$				
c_2	quadratic limb-darkening coeff	$0.333^{+0.049}_{-0.048}$				
Telescope Parameters:		FIES	Ondřejov	PARAS	TRES	Tautenburg
$\gamma_{\rm rel}$	Relative RV Offset (m/s)	29468^{+22}_{-20}	3549^{+77}_{-78}	-31^{+85}_{-84}	4571^{+21}_{-23}	-2766^{+43}_{-35}
σ_J	RV Jitter (m/s)	46^{+41}_{-30}	120 ± 120	230^{+100}_{-66}	40^{+43}_{-40}	$0.00^{+93}_{-0.00}$
σ_J^2	RV Jitter Variance	2200^{+5500}_{-1900}	13000^{+40000}_{-22000}	53000^{+57000}_{-26000}	1600^{+5300}_{-2200}	-1800^{+11000}_{-3500}
Transit Parameters:		TESS UT oi50-3.-TE (TESS)				
σ^2	Added Variance	$-0.0000000323^{+0.0000000064}_{-0.0000000063}$				
F_0	Baseline flux	0.9999834 ± 0.0000059				